

1 **Testing ground based observations of wave activity in the (lower and upper) atmosphere**
2 **as possible (complementary) indicators of streamer events**

3 **Michal Kozubek¹, Lisa Kuchelbacher², Jaroslav Chum¹, Tereza Sindelarova¹, Franziska**
4 **Trinkl^{2, a}, Katerina Podolska¹**

5 ¹Institute of Atmospheric Physics CAS, Bocni II 1401, Prague, 14100, Czech Republic

6 ² Earth Observation Center, Deutsches Zentrum für Luft- und Raumfahrt, 82234 Weßling,
7 Germany

8 ^a now at Karlsruhe Institute of Technology (KIT), Institute of Meteorology and Climate
9 Research, Karlsruhe, Germany

10 **Correspondence: Michal Kozubek, kom@ufa.cas.cz**

11 **Keywords:** gravity waves, streamer events, infrasound, Doppler measurements

12

13 **Abstract:** For a better understanding of atmospheric dynamics, it is very important to know
14 the general ~~condition~~[conditions](#) (dynamics and chemistry) of the atmosphere. Planetary waves
15 (PWs) are global scale waves, which are well-known as main drivers of the large-scale
16 weather patterns in mid-latitudes on time scales from several days up to weeks in the
17 troposphere. When PWs break, they often cut pressure cells off the jet stream. A specific
18 example are so-called streamer events, which occur predominantly in the lower stratosphere at
19 mid- and high-latitudes. For streamer events we check, whether there are any changes of
20 gravity wave (GW) or infrasound characteristics related to these events in ionospheric and
21 surface measurements (continuous Doppler soundings, two arrays of microbarometers) in the
22 Czech Republic.

23 Phenomena in infrasound arrival parameters undoubtedly related with streamer events were
24 not identified in observations of two stations located in Central Europe. Simulations of
25 infrasound propagation show influences of the streamer events on the waveguide formed near
26 the tropopause. Microbarom propagation is influenced by the tropopause waveguide in a
27 limited azimuth sector and at limited distances. Due to the typical occurrence of the streamer
28 events over the North Atlantic, infrasound stations in Western Europe can be of particular
29 interest for future studies of streamer event signatures in infrasound arrivals. Arrivals to
30 Central Europe are through the waveguide formed between the ground and the upper
31 stratosphere. The upper stratosphere waveguide is not influenced by the streamer events.

32 Supplementary ground-based measurements of GW using the WBCI array in the troposphere
33 showed that GW propagation azimuths were more random during streamer and streamer-like
34 events compared to those observed during calm conditions. GW propagation characteristics
35 observed in the ionosphere by continuous Doppler soundings during streamer events did not
36 differ from those expected for the given time period.

37

38 1) Introduction

39 For a better comprehension of climate change it is fundamentally important, how well we
40 understand the climate system in general, and the dynamics of the atmosphere in particular.
41 The dynamical processes [in the atmosphere](#) relevant in this context in the atmosphere take
42 place over a comparatively wide range of scales in space and time. They include in particular
43 both, planetary and gravity waves. Planetary waves are [one of](#) the main drivers of the
44 extratropical circulation. When they break, they lead to an irreversible exchange of air masses
45 between the equatorial and polar region due to an amplification of their amplitudes (e.g.
46 McIntyre & Palmer, 1983; Polvani & Plumb, 1992). In the lower stratosphere ozone can be
47 used as a tracer for these large-scale motions, as it has a comparatively long life-time. When
48 planetary waves break tropical air masses of low ozone concentration are mixed poleward into
49 the surrounding atmosphere of the mid and higher latitudes (e.g. Leovy et al., 1985).

50 The term "streamer" lacks a precise definition, as noted by Krüger et al. (2005). They
51 discuss various aspects of streamers, including their impact on mixing and the divergent
52 definitions associated with them. Offermann et al. (1999) describe streamers as large-scale
53 tongue-like structures formed by the meridional deflection of air masses. Streamers are
54 characterized by irreversible mixing of air masses between equatorial and polar regions which
55 is why they might be linked to planetary wave breaking (Vaughan, 1993). Eyring et al. (2003)
56 give a climatology of the seasonal and geographical distribution of streamer events. They
57 show, that streamers often occur over the Northern Atlantic and can be identified by either
58 high NO₂ or low ozone concentration, which is why we select streamers by total ozone
59 column measurements. [Eyring et al. \(2003\)](#) show that streamer events occur most often
60 during winter and least during July and August in the Northern Hemisphere. During a
61 streamer event the wind field changes rather [strongly](#) over a comparatively small
62 distance. Since a streamer event shows a strong wind shear at its flanks, it is expected that it
63 excites GW (e.g. Kramer et al., 2015 and 2016 or Peters et al., 2003).

64 It is well-known that enhanced wind gradients or anticyclones can lead to the
65 excitation of gravity waves (GW) in the atmosphere (e.g. Pramitha et al., 2015; Kai et al.,
66 2010; Kramer et al., 2015, 2016 and Gerlach et al., 2003). GW have typical vertical
67 wavelengths from a few 100 m to several kilometres (Wüst & Bittner, 2006), and horizontal
68 wavelengths over tens of km (Wüst et al., 2018), and longer (Rauthe et al., 2006); their
69 fluctuations in the upper troposphere / lower stratosphere typically show amplitudes of 5–10
70 m/s at maximum (e.g., Kramer et al., 2015). Those waves transport energy and momentum
71 horizontally and vertically through the atmosphere and deposit them especially in the
72 stratosphere and mesosphere but also above and below this height region. The propagation of
73 GWs is strongly dependent on the wind conditions in the stratosphere since the wind speed of
74 the middle atmosphere (10–100 km) reaches its maximum there. That is why monitoring
75 waves in upper parts of the atmosphere, e.g. based on Doppler observations in the ionosphere,
76 can provide additional information about stratospheric conditions (for details see Fritts and
77 Alexander, 2003).

78 Using pressure recordings at a microbarograph array, GWs and infrasound at the ground can
79 be observed. Ground based observations of GWs at a large aperture microbarograph array are
80 utilized in the present study as an independent data source for the analysis of GW activity
81 during streamer events. Infrasound propagation is influenced by wind and temperature fields
82 in the atmosphere. Three regions play an important role in long-distance infrasound
83 propagation: (1) the lower thermosphere; (2) the stratosphere; (3) the jet stream near the
84 tropopause and inversion layers in the troposphere (Evers and Haak, 2010). Infrasound
85 observed at the ground and emitted by distant sources mostly propagates in the stratospheric
86 waveguide (Ceranna et al., 2019). The thermospheric waveguide is not as efficient as the
87 stratospheric waveguide in the long-range infrasound propagation. Besides signal loss due to
88 geometrical spreading, infrasound absorption is important in the upper atmosphere (Bittner et
89 al., 2010). Infrasound absorption is proportional to the frequency; higher frequencies,
90 particularly those above 1 Hz undergo stronger absorption in the thermosphere (Sutherland
91 and Bass, 2004). Signal attenuation is low at frequencies of the order of $10^{-3} - 10^{-2}$ Hz (Blanc,
92 1985; Georges, 1968).

93 A number of case studies have proved that stratospheric dynamics can be deduced from
94 microbarograph measurements at the ground (Assink et al., 2014; Blixt et al., 2019; Evers and
95 Siegmund, 2009; Evers et al., 2012; Garcès et al., 2004; Le Pichon and Blanc, 2005; Le
96 Pichon et al., 2006 and 2009; Smets and Evers, 2014). Streamer events are significant

97 transient disturbances to circulation patterns in the tropopause/lower stratosphere region;
98 modifications of the stratospheric waveguide can therefore be expected. A feasibility study on
99 utilisation of ground infrasound measurements in research of streamer events is performed
100 [here](#). Its aim is to identify phenomena in infrasound detections related to the streamers; we
101 focus on deviations of the azimuth of signal arrivals, trace velocity, signal amplitude, and
102 frequency. ~~The dedicated~~[Dedicated](#) studies demonstrated that from the observed signal trace
103 velocity, information about the signal refraction height can be derived (Lonzaga, 2015). If the
104 source of received signals is well defined in time and space, mean atmospheric cross-winds
105 along the signal propagation path can be estimated from back-azimuth deviations and time of
106 signal propagation (Blixt et al., 2019). Fluctuations of signal frequency and amplitude are,
107 besides variability of the signal source influenced by atmospheric filtering (Sutherland and
108 Bass, 2004).

109 Our study will focus on [the](#) possible utilization Doppler sounding and microbarographs for
110 description and analysis of GW behaviour and propagation in the stratosphere.

111 The structure of the paper is as follows: After introduction the description of the used dataset
112 and method can be found in the second section. Then we describe our results and in the last
113 section we discuss the possible connection to previous studies.

114

115 **2) Data and methods**

116 The selection of streamer events is based on the visual inspection of global maps of total
117 ozone column ([TO3TCO](#)), accessible through a service provided by DLR
118 (<https://atmos.eoc.dlr.de/>) measured by the Tropospheric Monitoring Instrument (TROPOMI)
119 aboard the Sentinel 5 Precursor (S5P) mission. See Veefkind et al., 2012 for details about
120 TROPOMI/S5P. In cases where TROPOMI/S5P data is unavailable, measurements from the
121 Global Ozone Monitoring Experiment-2 (GOME-2) on the Metop series of satellites are
122 utilized. Both instruments operate in a nadir-viewing configuration on near-polar sun-
123 synchronous orbits. Further specifics regarding [TO3TCO](#) measurements by TROPOMI/S5P
124 are elaborated by Spurr et al. (2022). The [TO3TCO](#) retrieval process is built upon the
125 predecessor instrument's processor, with GOME-2 on Metop-AB, see Munro et al. (2006) and

126 Munro et al. (2016). For detailed information on the GOME-2 retrieval algorithm, refer to
127 Loyola et al. (2011).

128 We define a streamer as such when the ozone column concentration of the finger-like
129 structure above the Northern Atlantic/Western Europe is lower than 300 DU and persists for
130 at least 3 days. The longitudinal extension is of approx. 15 to 30 degrees in the mid-latitudes
131 (between 30 to 70°N). The northernmost point of a streamer exceeds 50°N. Fig. 1 shows a
132 streamer event above the Northern Atlantic, indicated by the blue color which represent the
133 low ozone concentrations. The streamer shown in Fig. 1 reaches latitudes beyond 70°N,
134 which indicates a large example. At the western and eastern flanks of the streamer, the ozone
135 concentration exceeds 350 DU, defining distinct boundaries. This is also visible in Fig. 1
136 represented by the green colors at the eastern coast of Northern America and western Europe.
137 So, there is a gradient of the ozone concentration of about 50 DU / 5°. Furthermore, the
138 streamer exhibits a discernible pattern of circulation, with air masses being meridionally
139 deflected, contributing to its formation and maintenance. These air masses, characterized by
140 their movement from south to north at the eastern flank and from north to south at the western
141 flank, play a significant role in the streamer's dynamics. This is the reason why equatorial low
142 ozone concentration is transported northward. In contrast, the calm periods, representing the
143 opposite dynamic situation to the streamer events, are characterized by only very few
144 meridionally deflected air masses. During these periods, the ozone concentration in the mid-
145 latitudes above the Northern Atlantic is consistently higher than 350 DU, indicating stable
146 atmospheric conditions and minimal perturbations in the ozone distribution. An example for a
147 calm period is shown in Fig. 2.

148 The streamer events are selected by eye for this study (results see Table 1) considering the
149 TO3 global maps from January 2020 and March 2021. As planetary waves are permanently
150 disturbing the atmospheric dynamic of the higher troposphere / lower stratosphere, especially
151 smaller scale streamers can be observed almost every day and the identification of streamer
152 events becomes subjective. We therefore focus on few events which are comparatively strong
153 in their evolution from our perspective. Moreover, we focus on streamer events above the
154 Northern Atlantic. Whenever another streamer event occurs somewhere other than over the
155 Northern Atlantic region with comparable spatiotemporal extent, we do not consider this date
156 as a streamer event. We assume that the effects of the streamer superimpose and a distinct
157 backtrack to the streamer over the Northern Atlantic will not be possible. This means, that the
158 analysis of the streamer events can be blurred to some extent.

159 We consider dates from January 2020 to April 2021. In general, planetary waves drive the
 160 Brewer Dobson Circulation in the stratosphere during winter and ozone-poor airmasses are
 161 transported northward. Streamer events are therefore detected between September and March.
 162 The streamer events are distinguished if they have a large spatial size, high intensity (low
 163 TO3 concentration) and if air masses are irreversibly mixed into the surrounding atmosphere.
 164 All the selected events persist for several days, but no longer than 10 days.

165 To evaluate whether streamer events effect the smaller-scale atmospheric dynamics, calm
 166 events are identified as well by subjective criteria. These events serve as a reference to
 167 streamer events, as large-scale spatial structures are hardly visible in the TO3. The events are
 168 selected when the ozone concentration shows a meridional gradient from the equator to [the](#)
 169 polar region on the Northern Hemisphere with almost no longitudinal variation. The examples
 170 of calm atmospheric dynamics are listed in Table 1 (right).

171

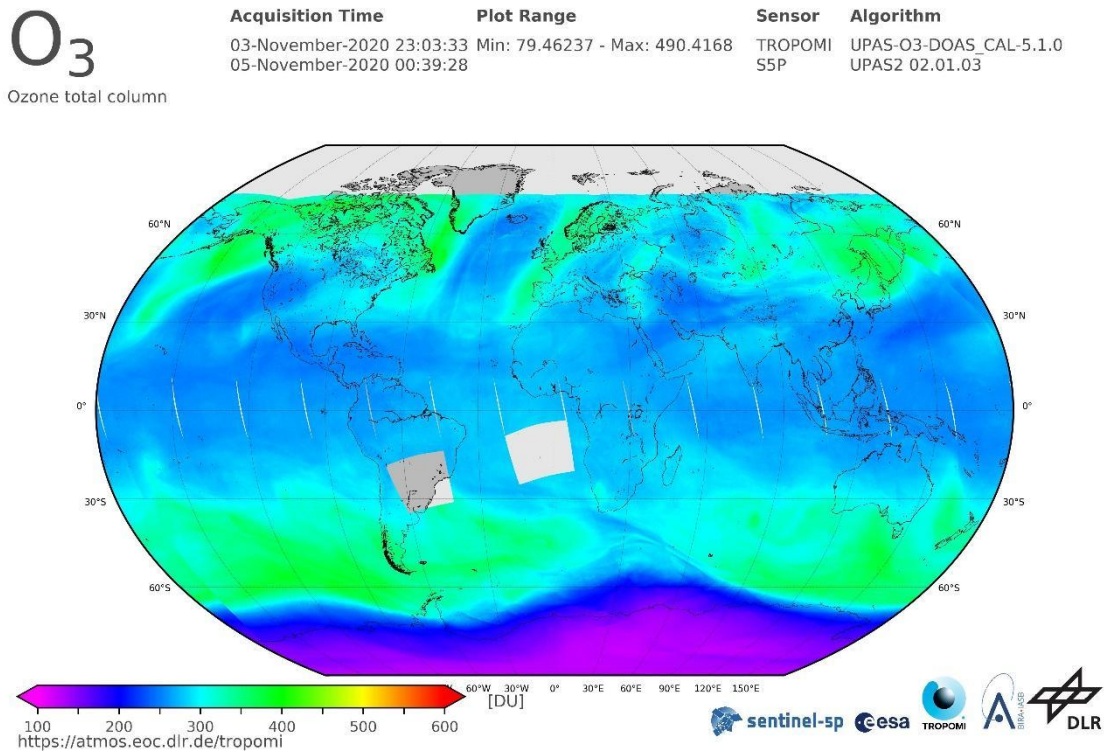
Streamer events		Calm periods	
From	To	From	To
06.02.2020	10.02.2020	02.03.2020	08.03.2020
11.2.2020	13.2.2020	09.03.2020	14.03.2020
31.08.2020	03.09.2020	28.03.2020	10.04.2020
05.09.2020	11.09.2020	19.04.2020	27.05.2020
03.11.2020	07.11.2020	9.11.2020	15.11.2020
21.11.2020	25.11.2020	12.12.2020	22.12.2020
23.02.2021	27.02.2021	30.12.2020	06.01.2021
09.03.2021	12.03.2021	21.01.2021	20.02.2021
		28.02.2021	07.03.2021
		13.03.2021	24.03.2021
		29.03.2021	07.04.2021

--	--	--	--

172 **Table 1** Streamer events above Northern Atlantic from January 2020 until March 2021 and
 173 related start and end dates. The right part shows calm periods.

174

175 Figure 1 shows the [TO3TCO](#) by TOPOMI/S5P integrated from November 3rd to November
 176 5th 2020. Ozone-poor airmasses (blue) are located above the Northern Atlantic from 30°N to
 177 70°N next to smaller scale ozone-poor airmasses above western North America and Central
 178 Asia. The TO3 concentration is disturbed by planetary waves along the latitudes, which lead
 179 to wave structures visible especially at the transition of blue to green colors. A large streamer
 180 event of ozone-poor airmasses is detected over the Northern Atlantic. A small streamer can be
 181 detected over western North America. There are also ozone-poor air masses above eastern
 182 Europe. The temporal evolution shows, that the ozone-poor air masses above eastern Europe
 183 are due to a decaying streamer which evolved several days earlier. As planetary waves are
 184 more or less permanently disturbing the atmospheric dynamics, especially smaller scale
 185 streamers can be detected almost every day. In this example, the streamer event above the
 186 Northern Atlantic is largest. Therefore, we consider this event for the further analysis.

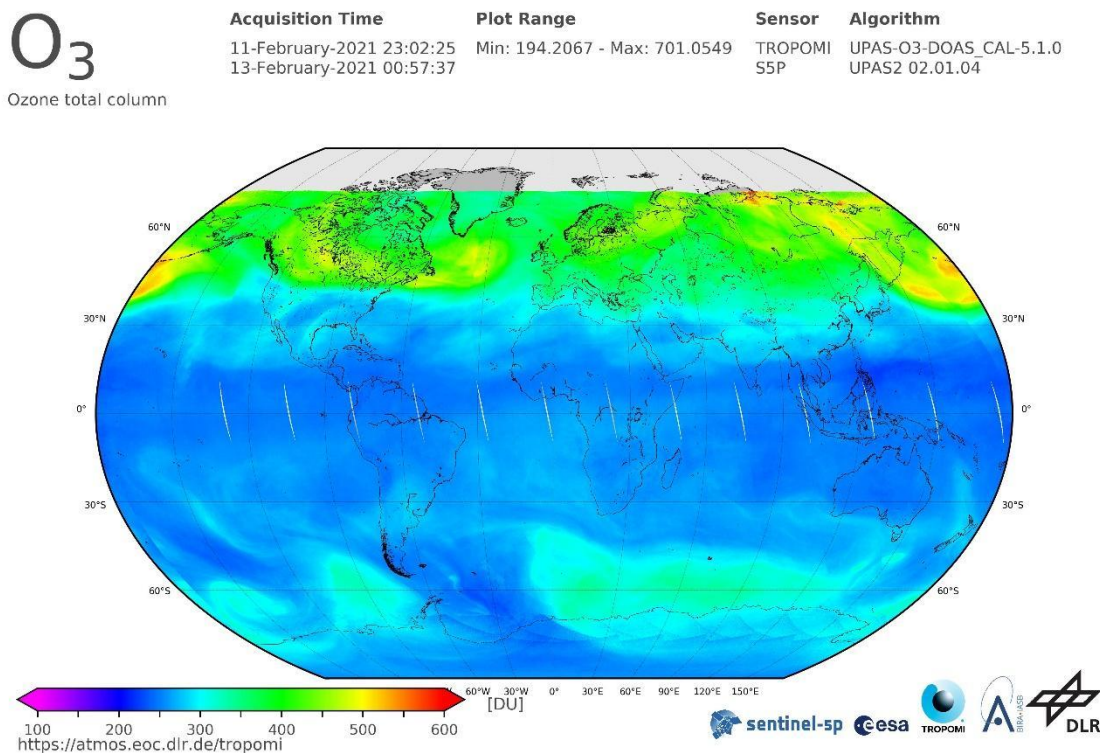


188 Fig. 1. [T₀₃TCO](#) by TROPOMI/S5P from November 3rd to November 5th 2020 shows ozone
 189 poor airmasses above the Northern Atlantic as an example of a streamer event for the further
 190 analysis. Colors (from violet to red) indicate the total ozone column concentrations (from low
 191 to high) in Dobson Units. Source: DLR, CC-BY 3.0

192

193 Figure 2 shows the [T₀₃TCO](#) by TOPOMI/S5P from February 11th to February 13th 2020.
 194 The event is characterized by a strong meridional gradient from the equatorial to polar region
 195 on the Northern Hemisphere with almost no longitudinal variation. Therefore, we consider
 196 this event for the further analysis.

197



198

199 Fig. 2. [T₀₃TCO](#) by TROPOMI/S5P from February 11th to February 13th 2020 as an example
 200 of calm atmospheric dynamics. A clear meridional gradient of ozone can be observed on the
 201 Northern Hemisphere without large-scale wave structures. Colors (from violet to red) indicate
 202 the total ozone column concentrations (from low to high) in Dobson Units. Source: DLR, CC-
 203 BY 3.0

204 Two stations of the Czech microbarograph network (Bondar et al., 2022) are involved in the
 205 study – the large aperture array WBCI (50.25°N 12.44°E) and the small aperture array PVICI
 206 (50.52°N 14.57°E). To study propagation of GW and long-period infrasound (from acoustic
 207 cut-off up to about 2.5 s) pressure recordings at WBCI are utilized. Four sensors of the WBCI
 208 array are arranged in a tetragon. The inter-element distances of 4 – 10 km define an optimum
 209 performance of the array in the infrasound frequency range from the acoustic cut-off

210 frequency of 0.0033 to 0.0068 Hz (Garcès, 2013). The WBCI array with its large inter-
 211 element distances has a unique configuration compared to the arrays of the International
 212 Monitoring System of the Comprehensive Nuclear Test Ban Treaty Organisation intended
 213 for infrasound monitoring in the frequency band of 0.02 – 4 Hz (Marty, 2019). Each array
 214 element at WBCI is equipped with an absolute microbarometer of the type Paroscientific
 215 6000-16B-IS with parts-per-billion resolution. A GPS receiver is used for time stamping. Data
 216 are stored with a sampling rate of 50 Hz. For infrasound monitoring, WBCI data are
 217 resampled at 10 Hz sampling rate. To detect and analyze GW, 1-min mean values of the
 218 absolute pressure data are used.

219 The small aperture array PPCI provides optimal precision of detections in the frequency
 220 range of 0.14 – 3.4 Hz (Garcès, 2013). Three sensors are arranged in an equilateral triangle;
 221 the array aperture is 200 m. The differential sensors of the type Infrasound Gage ISGM03
 222 manufactured by the Scientific and Technical Centre give a flat response in the frequency
 223 range of 0.02 – 4 Hz. A GPS receiver is used for time stamping. The data are stored with a
 224 sampling frequency of 25 Hz. This sampling rate is also used in regular processing of
 225 infrasound detections at PPCI.

226 Infrasound detections are processed using the DTK-GPMCC software the core of which is the
 227 Progressive Multi-Channel Correlation (PMCC) detection algorithm (Cansi, 1995; Le Pichon
 228 and Cansi, 2003). PMCC analyses pressure recordings from an infrasound array and looks for
 229 coherent signals in overlapping time windows in several frequency bands (Le Pichon and
 230 Cansi, 2003). An elementary detection with the PMCC, or the detection pixel is declared in
 231 the time-frequency window, when signal correlation and consistency criteria are met.
 232 Detection pixels are grouped into the detection families based on similar time, frequency,
 233 azimuth of signal arrival, and signal trace velocity (Brachet et al., 2010). The arrival
 234 parameters of the detected infrasound are stored in the detection bulletins. The parameters of
 235 interest for the present study include time of arrival, azimuth of arrival, trace velocity,
 236 frequency, and amplitude. The PMCC configuration is set on an individual basis and is
 237 optimized for the given array (Brachet et al., 2010; Garcès, 2013; Szuberla et al., 2004); main
 238 parameters of the DTK-GPMCC settings for the arrays PPCI and WBCI are given in Table 2.

Station	PPCI	WBCI
Detection range	0.09-7 Hz	0.0033-0.4 Hz
Number of detection bands	19	11

Length of the detection window; frequency dependent	412.84-6.44 s	2555-118 s
Adjacent windows overlap	95 %	90 %
Consistency	0.1 s	3 s
Azimuth tolerance for families forming	10°	3°
Family size	10-50 pixels	15-50 pixels
Frequency range analysed in the study of streamer events	0.09-0.4 Hz	0.0033-0.4 Hz

239

240 **Table 2.** Main parameters of the DTK-GPMCC configurations for the arrays PPCI and
241 WBCI.

242

243 InfraGA/GeoAc raytracing tools are employed to study infrasound ducting in the atmosphere
244 (Blom and Waxler, 2012; Blom, 2019). Infrasound raytracing [provides an easy-to-interpret](#)
245 [approximation of infrasound propagation and](#) can ~~reveal~~[help to identify](#) possible
246 modifications of atmospheric waveguides above ~~the~~ Eastern Atlantic and Western Europe
247 during streamer events. ~~Streamer events influence and it can show whether the streamer event~~
248 [influences reach Central Europe. The raytracing is employed in our study for the tropopause](#)
249 [and lower stratosphere. Hence, modifications of the stratospheric waveguide are expected](#)
250 [rather than its entire reversals or collapse. Raytracing can identify purpose of identifying](#)
251 azimuths and distances from the source that ~~are~~[can be](#) influenced by ~~at~~[the](#) streamer event. And
252 so, it can reveal whether these influences reach Central Europe or the signals are ducted to the
253 region through the waveguide in the upper stratosphere or thermosphere like in quiet periods.
254 InfraGA/GeoAc provides simulations of signal propagation from a point source; propagation
255 through the range dependent atmosphere is modelled in the present study. Atmospheric
256 characteristics are obtained from the G2S model (Drob et al. 2003). Vertical profiles of
257 temperature, zonal and meridional winds, density and pressure are an input for the
258 InfraGA/GeoAc. The grid of profiles covers the area from 45° to 65°N and from 30°W to
259 22.5°E; latitudinal step is 5° and longitudinal step is 7.5°.

260 Propagation of GW in the thermosphere/ionosphere is studied using the multi-point and multi-
261 frequency continuous Doppler sounding system located in Czechia. Its advantage is a high
262 time resolution (around 10 s) compared with ionospheric sounders (ionosondes) that measure

263 the profile of electron densities in the ionosphere. The frequency shift is due to the motion and
264 electron density changes in the ionospheric plasma, caused for example by interaction with
265 atmospheric waves propagating in the neutral atmosphere, with which the ionosphere (above
266 ~ 80 km) merges. The sounding radio signal is reflected at the height, where its frequency
267 matches the so called local plasma frequency, which is determined by the local electron
268 density. Therefore, the reflection height changes during the day and depends on the sounding
269 frequency. Significant Doppler shifts, usable for analysis, are obtained if the signal is
270 reflected from the so called [ionospheric](#) F2 layer (approximately 200 – 300 km). Several
271 sounding frequencies are used in Czechia. The 3.59 MHz sounding was mostly effective at
272 night, while the 4.65 MHz sounding provided good daytime data during the period analyzed.
273 The propagation characteristics of GWs are calculated from the time delays between signals
274 observed at the respective sounding paths (reflection points for each transmitter-receiver
275 pairs) assuming that the reflection points are in the midpoints between each transmitter and
276 receiver. A 60 or 90 min long time interval is usually used to calculate the velocities and
277 azimuth of the observed waves. The methods are in detail described by Chum and Podolska
278 (2018). The two-dimensional (2-D) version (propagation analysis in horizontal plane only) is
279 anticipated for most of the studies, since a 3-D analysis requires simultaneous observation and
280 signal correlation at different frequencies, which is often not the case, especially during solar
281 minimum. Results of statistical investigation have been recently published (Chum et al.,
282 2021). Identical methods of propagation analysis have been applied to investigate
283 propagation of GWs in the troposphere based on data from large-aperture array WBCI (here
284 the time delays are related to the locations of individual microbarometers). All analyses will
285 be done with respect to the streamer events and calm periods shown in Table 1.

286 **3) Results**

287 **3.1 Infrasound observations at ground microbarograph arrays WBCI and PPCI in** 288 **November 2020 and in March 2021**

289 Wave activity in the infrasound frequency range of 0.0033-0.4 Hz is investigated combining
290 observations at the stations WBCI and PPCI. Infrasound detections at WBCI are processed in
291 the frequency band of 0.0033 – 0.4 Hz. The operational range of the array is extended above
292 the upper limit of the optimum array range; the degraded performance of WBCI at
293 frequencies higher than 0.0068 Hz shall be considered. The upper limit of the analysed band
294 is intentionally set to 0.4 Hz to cover microbaroms. PPCI detections are analysed in the

295 frequency range of 0.09 – 0.4 Hz. The band partly overlaps with the detection range of the
296 WBCI array and at frequencies of 0.12 – 0.35 Hz it is dominated by microbaroms (e.g.,
297 Campus and Christie, 2010). Unlike WBCI, PSCI provides an optimal performance in the
298 microbarom band.

299 Microbaroms are infrasound signals generated by a non-linear interaction of ocean waves
300 travelling in opposite directions. Microbaroms form a wide peak around 0.2 Hz in the
301 infrasound spectrum; their frequency corresponds to twice the frequency of sea waves. A
302 powerful source of microbaroms is located in the North Atlantic and the signals are regularly
303 detected by European stations (Hupe et al., 2019). The detection capability of microbaroms
304 from the North Atlantic is particularly high from October to March when the source becomes
305 stronger due to stormy weather above the ocean and signal propagation to the East from the
306 source is supported by the stratospheric waveguide (Landès et al., 2012). From the global
307 point of view, microbaroms are permanently present in recordings of infrasound stations
308 worldwide.

309 Streamer events often occur above the North Atlantic. Thus, microbaroms propagating from
310 the North Atlantic to the continental Europe can travel through the region influenced by a
311 streamer event and the detections at infrasound stations in Europe can show signatures of
312 streamer events.

313 We analyse infrasound observations from 3rd to 25th November 2020 and from 28th
314 February to 25th March 2021 with focus on microbaroms. In these time intervals adjacent
315 streamers and calm periods occurred (Table 1). [Streamers](#) and the calm
316 period in the November 2020 time window are evaluated separately from those in the
317 March 2021 time window to avoid seasonal influences. While a well-developed eastward
318 stratospheric waveguide can be expected in November, its efficiency can decrease in March
319 due to the seasonal reversal of stratospheric winds.

320

321 **3.1.1 Infrasound observations from 3rd to 25th November 2020**

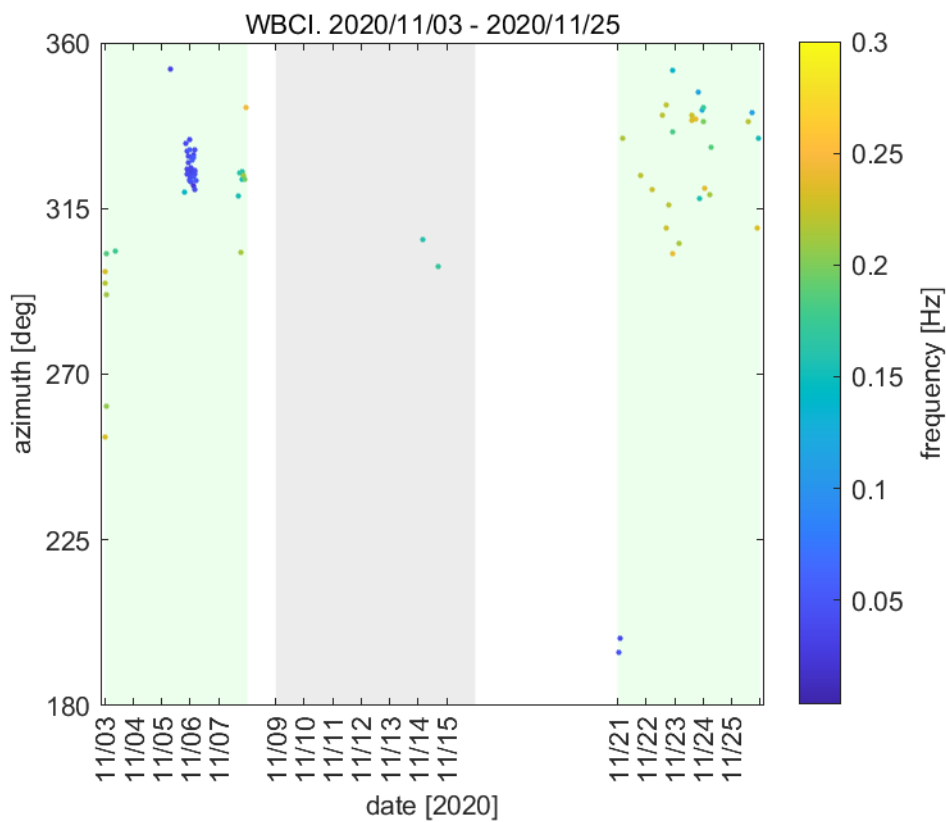
322 Two streamer events developed in November 2020. The first streamer occurred from 3rd
323 to 7th November and the second one from 21st to 25th November. The streamers were
324 separated by a calm period from 9th to 15th November.

325 The most important phenomena found in the infrasound arrival parameters are fluctuating
326 signal frequency and fluctuating signal amplitude.

327 WBCI provides rather sparse detections during both streamer events and only two
328 detection families are obtained during the seven-day calm period (Figure 3). The [signal](#)

329 frequencies near 0.2 Hz and back-azimuths of $290^{\circ} - 350^{\circ}$ indicate that the observed
 330 signals are likely microbaroms from the North Atlantic. A decrease of the signal frequency
 331 is observed during the first streamer event. On 5th – 6th November from 20 to 05 UTC, the
 332 mean frequency of the north-west arrivals drops down to 0.04 Hz, below the microbarom
 333 frequency range. During the second streamer event from 21st to 25th November, the signal
 334 frequency is stable around 0.22 Hz. An increase of the amplitude from the mean value of
 335 0.019 Pa to 0.035 Pa is observed from 23rd November, 18 UTC until the end of the analysed
 336 time period on 25th November at 24 UTC.

337



338

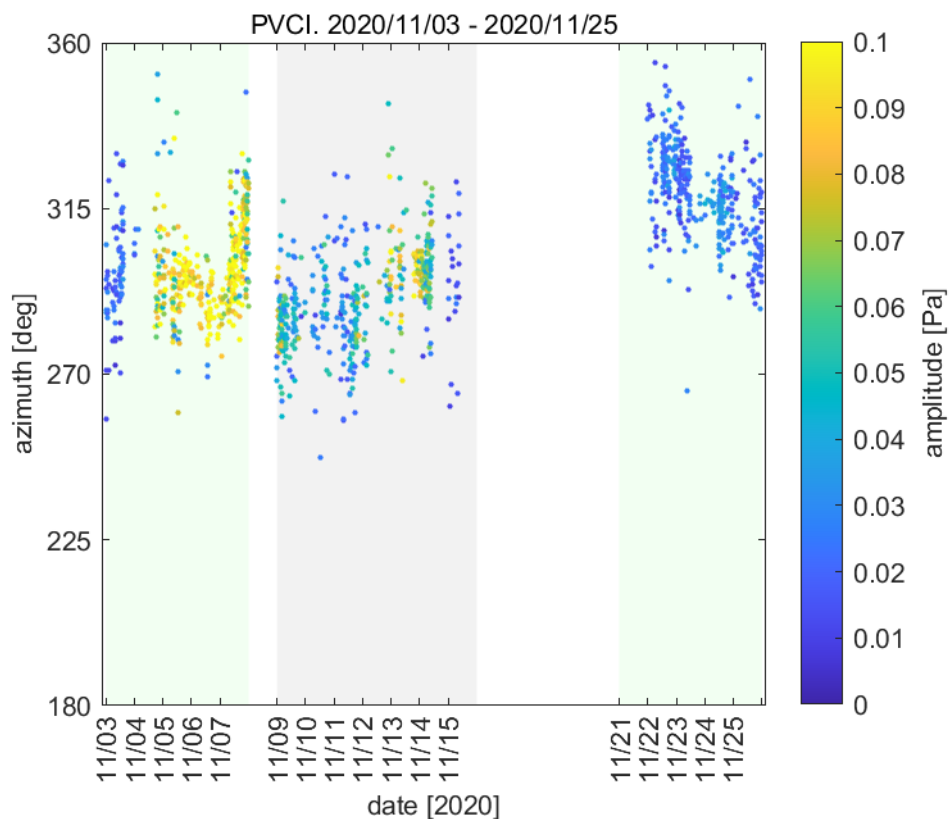
339 Fig. 3. Infrasound observations at WBCI on 3rd - 25th November 2020. Azimuth of signal
 340 arrivals is shown; the colorbar refers to the mean frequency of the detection family. One circle
 341 in the plot represents one detection family. Green background marks the streamer events, grey
 342 background marks the calm period.

343

344 Similar to the back-azimuths at WBCI, PNCI detects arrivals from the north-west in the
 345 analysed frequency range of 0.09 – 0.4 Hz (Figure 4). Fluctuating signal amplitudes are
 346 observed. Values around 0.020 Pa occur on 3rd November. From 4th November, 18 UTC to 7th
 347 November, 22:30 UTC, the signals are of amplitudes around 0.089 Pa. The amplitudes

348 decrease to the values around 0.046 Pa during the following quiet period on 9th – 15th
 349 November. Microbarom amplitudes fluctuate between 0.013 and 0.036 Pa (1st decile and 9th
 350 decile, respectively) during the streamer event on 21st – 25th November. Publicly available
 351 data –such as meteorological charts provided by Deutscher Wetterdienst and the
 352 WAVEWATCHIII® wave-action model (The WAVEWATCHIII® Development Group,
 353 2016) indicate that there are maritime storms in the North Atlantic within the analysed time
 354 window from 3rd to 25th November 2020. [Maximum heights of sea waves are predicted in the
 355 North Atlantic near south coast of Greenland and Island from 5th to 6th November, from 12th
 356 to 13th November, and on 20th November. The storms can cause height of combined wind
 357 waves and swell reaches 10 m. As mentioned in section 3.1 it is not only the wave height but
 358 also the wave direction \(waves propagating in opposite directions\) that determines the
 359 microbarom source. Nevertheless, fluctuating intensity of the microbarom source ~~and as shall~~
 360 be taken into account during maritime storms. As a consequence, fluctuating microbarom
 361 amplitudes ~~are can be~~ observed at the infrasound stations.](#)

362
 363
 364



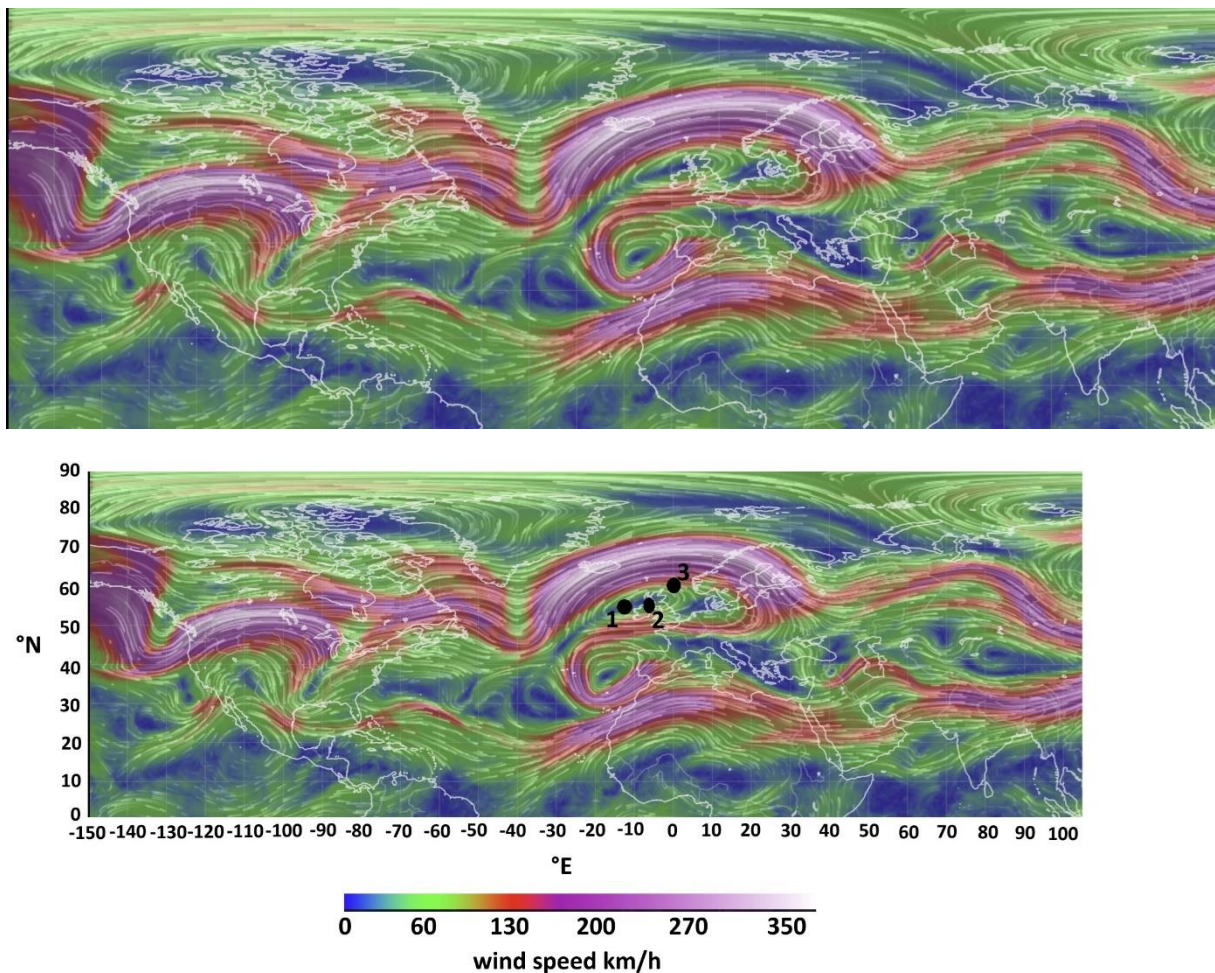
365

366 Fig.4. Infrasound observations at PPCI on 3rd - 25th November 2020. Azimuth of signal
367 arrival is shown; the colorbar refers to the signal amplitude. Green background marks the
368 streamer events, grey background marks the calm period.

369

370 To study propagation of signals from sources located at the surface of the North Atlantic
371 the InfraGA/GeoAc tools are employed. The fictitious point sources are located (1) at 55°N
372 and 15°W, (2) at 55°N and 5°W, and (3) at 60°N and 0°longitude. The coordinates of the
373 sources are estimated based on the position of the tropopause jet stream disturbance. Point
374 (1) is located under the northward jet-stream, point (3) under the southward jet-stream, and
375 point (2) is located between those two opposing branches of the jet stream disturbance, see
376 Figure 5.

377



378

379

380 Fig.5. Wind field at the pressure level of 250 hPa on 06 November 2020 at 00 UTC. A
381 disturbance of the jet-stream above the eastern North Atlantic and the British Isles is caused
382 by the streamer event. [Figure taken from earth.nullschool.net](http://earth.nullschool.net)

383

384 A multi azimuth simulation is run on 6th November at 00 UTC, during. The simulation is
385 performed at the time point in the middle of the streamer event when a maximum stage of the
386 phenomenon can be expected. Taking into account the mutual locations of the sources and the
387 receiving arrays, eastward signal propagation is modelled. The azimuth limits are set to 0° and
388 180° , the azimuth step is 3° . Signal Rays are launched with inclinations of 2° – 45° are
389 considered in $^\circ$; the step is 2° resolution. $^\circ$.

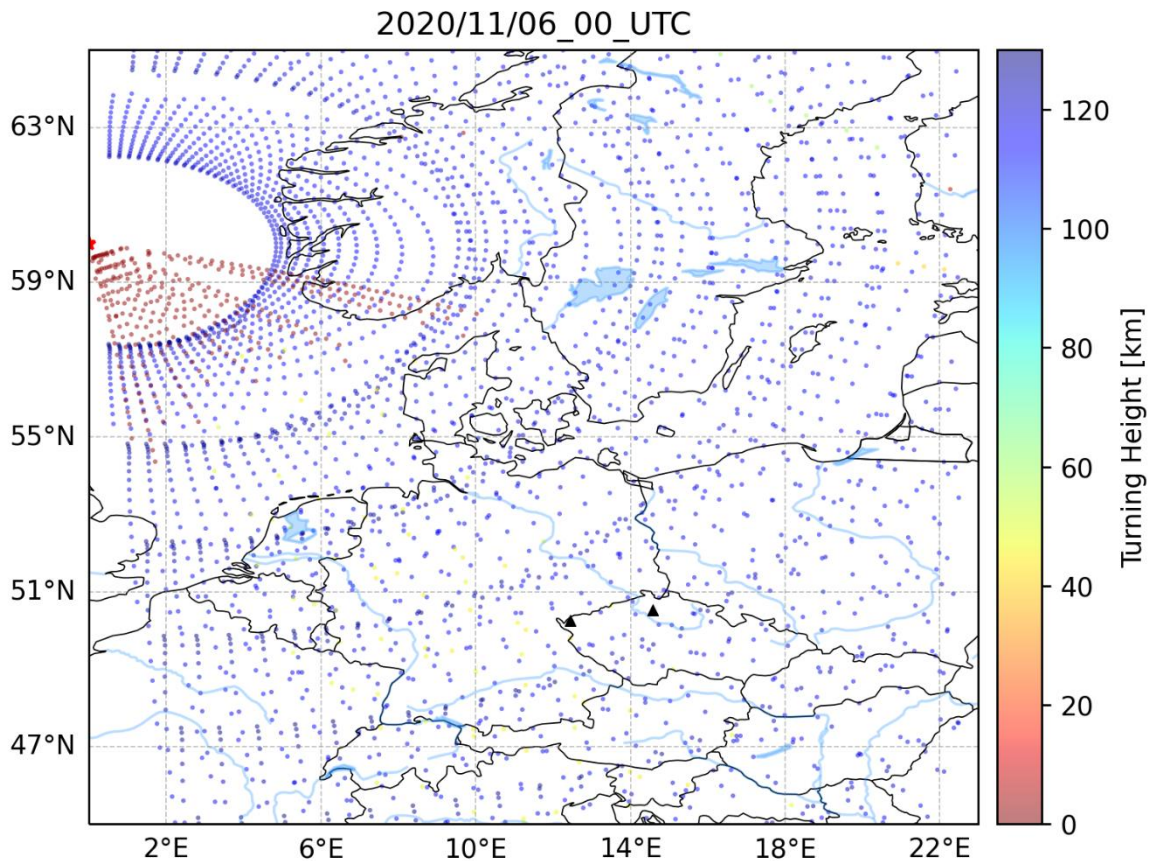
390 Information is obtained through which waveguides the signal can possibly arrive to the
391 infrasound stations and their surroundings. The reason why arrivals to extended areas around
392 the larger areas stations are considered is that signal propagation from three fictitious point
393 sources stands in for an area a real source, the surface of the North Atlantic where
394 microbaroms are generated. Therefore, the model outputs must be taken as an approximation
395 of the real situation. The turning height and ground reflections of the 0.2 Hz signal are
396 obtained in the multi azimuth simulation. The results are visualised in Figure 6 and in
397 supplementary materials. The red asterisk represents the point source. The concentric sectors
398 of circles show i.e. regions of ensonification, regions where the signal emitted by the source
399 can be recorded at an infrasound station. The dots, showing signal ground reflections are
400 organized in a radial pattern. Each of the lines of this pattern represents one azimuth of signal
401 propagation for which the multi azimuth simulation is run; the azimuth step is 3° . The colours
402 of the dots inform about the turning height of the ray and thus provide information about
403 signal ducting in the waveguides. Depending on the turning height, infrasound is subject to
404 attenuation of variable strength when it propagates through the atmosphere. Infrasound
405 attenuation is low in the stratospheric waveguide. Strong absorption occurs in the
406 thermospheric waveguide; the absorption is higher at higher signal frequencies (Sutherland
407 and Bass, 2004). To obtain the view of signal attenuation along the raypath in the vertical
408 plain a single azimuth simulation is employed. The single azimuth simulation is run along the
409 azimuths from the fictitious sources (1) – (3) to the stations WBCI and PPCI; it is obtained
410 for the frequencies of 0.04 Hz and 0.2 Hz. As a reference, a multi azimuth propagation of the
411 0.2 Hz signal is modelled from a source at 55°N and 15°W on the calm day 12th November at
412 00 UTC. The time point in the middle of the calm period between two streamer events is
413 selected to minimize possible effects of the subsiding and arising streamer event, respectively.
414 First, we focus on infrasound propagation from the North Atlantic to Central Europe. Signal
415 arrivals only through the thermospheric waveguide are enabled from the source at 60°N and
416 0° longitude (Figure 6) during the streamer event on 6th November 2020 at 00 UTC.

417 Stratospheric and thermospheric ducting are possible from the sources at 55°N 15°W and
418 55°N 5°W to Central Europe [during\(supplementary materials\)](#). Similarly, stratospheric and
419 [thermospheric ducting is predicted from](#) the [streamer event as well as source at 55°N 15°W to](#)
420 [Central Europe](#) on the calm day [12th November 2020](#) (supplementary materials). Signal
421 propagation only through the thermospheric waveguide is enabled from the source at 60°N
422 and 0°longitude (Figure 6). The distances between the fictitious sources and the stations are
423 1300 – 2000 km. The amplitude loss of the 0.2 Hz signal in the thermospheric waveguide at
424 these distances is 100 dB relative to the amplitude at a distance of 1 km from the source.
425 According to the simulations, observations of the thermospheric arrivals of microbaroms are
426 unlikely at PPCI and WPCI due to strong signal attenuation. Microbaroms apparently arrive
427 to Central Europe through the [stratospheric](#) waveguide formed in the upper stratosphere
428 during the streamer events as well as on the calm day. Indeed, arrivals from the back-azimuths
429 of 285° - 315° are dominant at PPCI [from](#) 3rd to 7th November. Those back-azimuths
430 correspond to the [positions of the fictitious](#) sources at 55°N 15°W and at 55°N 5°W, while the
431 back-azimuth to the source at 60°N and 0°latitude is 325°. The amplitude loss of the 0.04 Hz
432 signal at the distances of 1300 – 2000 km from the source is 60 – 80 dB. In general,
433 thermospheric arrivals of this low frequency signal are not strictly rejected. However, in our
434 case the 0.04 Hz signal arrives with trace velocity around 0.330 km/s at WPCI. The low trace
435 velocity indicates signal [ductingpropagation](#) in the troposphere/lower stratosphere waveguide
436 (Lonzaga, 2015).

437 Next, we study the influences of the streamer event related disturbance anywhere in the
438 modelled region. The disturbance of the jet stream can modify signal propagation up to
439 distances of several hundreds to a thousand km from the source; the influenced azimuth
440 range is limited. Signals from the source at 55°N and 15°W can propagate in the tropopause
441 waveguide in azimuths between 10° and 60° up to the distance of ~1000 km. The amplitude
442 loss of the 0.2 Hz signal at a distance of 1000 km is 60-70 dB relative to the amplitude at 1
443 km from the source. The southward branch of the jet-stream disturbance enables infrasound
444 propagation in the tropospheric waveguide in azimuths of 100 - 160° from the source at
445 60°N 0°longitude. Maximum distance which the signal can travel in the south-east direction
446 is ~600 km. The amplitude loss of the 0.2 Hz signal at a distance of 600 km is 60 dB
447 relative to the amplitude at 1 km from the source.

448 The observations and the model outputs during the November 2020 event can be
449 summarized as follows: infrasound arrives from sources in the North Atlantic to Central
450 Europe mainly through the stratospheric waveguide formed between the ground and upper

451 stratosphere. The jet-stream disturbance above the eastern North Atlantic does not have an
 452 impact on infrasound arrivals in Central Europe on 6th November 2020 at 00 UTC.
 453 Fluctuating signal amplitudes are likely a consequence of fluctuating intensity of the
 454 microbarom source during maritime storms. The decrease of signal frequency at WBCI is
 455 not caused by a transient change in signal ducting and by the related signal filtering in the
 456 thermospheric waveguide.
 457



458
 459 Fig.6. Modelled infrasound propagation from a point source located at 60°N and 0°longitude
 460 (red asterisk) during the streamer event on 6th November 2020 at 00 UTC. [Colorbar](#)The
 461 [colorbar](#) refers to the turning height (maximum height) of the signal. Red [color](#) indicates
 462 signal propagation in the waveguide formed near the tropopause (altitudes around 10 km),
 463 arrivals through the thermospheric waveguide are [shown](#) in blue (altitudes above 100 km).
 464 Black triangles represent infrasound arrays WBCI (the left triangle) and PVICI (the right
 465 triangle).

466

467 3.1.2 Infrasound observations from 28th February to 24th March 2021

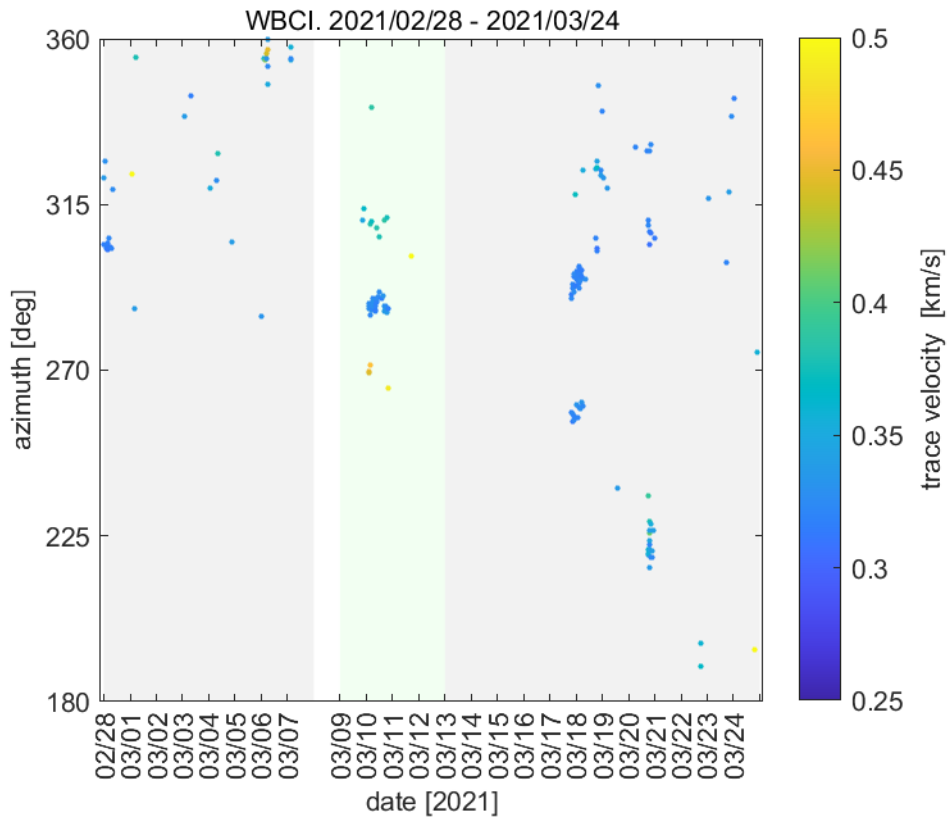
468 [Another](#) streamer event occurred from 9th to 12th March 2021 preceded and followed by
469 calm periods from 28th February to 7th March and from 13th to 24th March, respectively.

470 The most important phenomenon identified in the infrasound arrival parameters is a
471 fluctuating trace velocity.

472 Both WBCI and PPCI detect signals arriving from the north-west, from back-azimuths of
473 285° – 310°. An increase of signal trace velocities is observed in some of the detections at
474 WBCI during the streamer event compared to calm periods (Figure 7). On 10th March at 00 –
475 06 UTC, trace velocities of 0.460 km/s and 0.380 km/s are observed from back-azimuths of
476 270° and 310° respectively. It is by 0.05 – 0.13 km/s higher than on the calm days. On the
477 other hand, signals from the back-azimuth of 288° arrive with the trace velocity of 0.330 km/s
478 within the same time window, ~~the~~[this](#) velocity corresponds to that on the calm days. Effects
479 of spatial aliasing shall be taken into account when evaluating the detections. The signal
480 frequencies are around 0.2 Hz, well above the range of array optimum performance. The
481 observed different trace velocities at WBCI can therefore be a processing bias rather than a
482 consequence of variations in signal ducting.

483 In contrast to the WBCI observations, PPCI records a decrease in trace velocities on 10th
484 March at 00 – 06 UTC (Figure 8). Trace velocities of 0.377 km/s are observed compared to
485 0.413 km/s and 0.395 km/s during the calm periods before and after the streamer,
486 respectively.

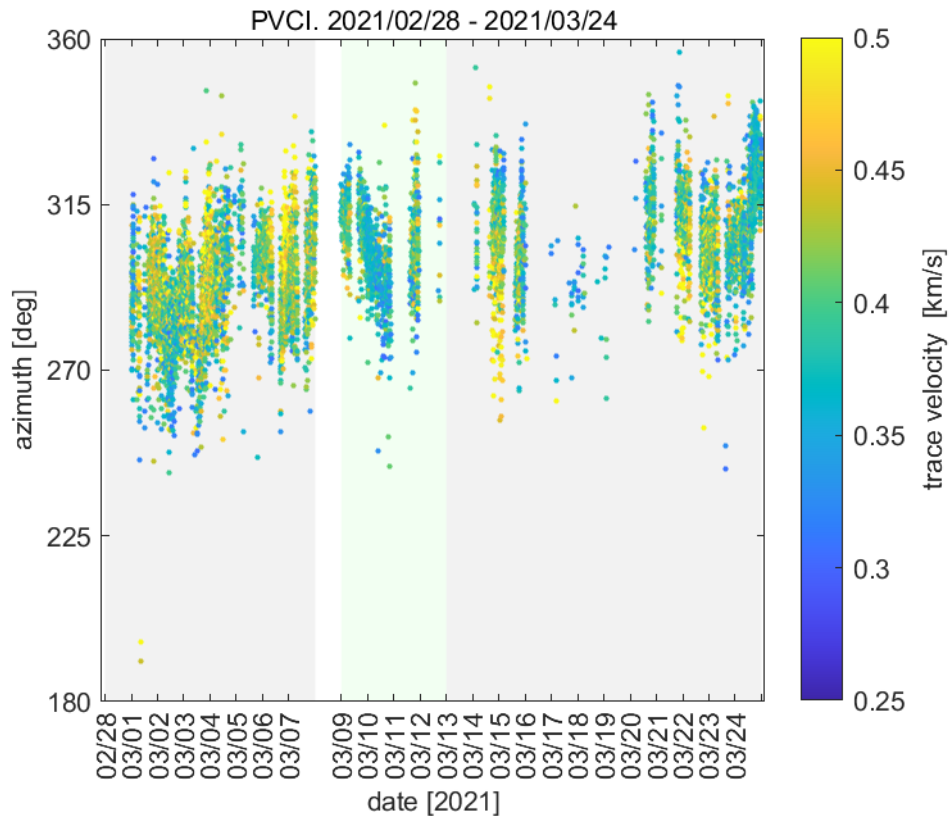
487



488

489 Fig.7. Infrasound observations at WBCI on 28th February – 24th March 2021. Azimuth of
 490 signal arrival is shown; the colorbar refers to the signal trace velocity. Green background
 491 marks the streamer event, grey background marks the calm periods.

492



493

494 Fig.8. Infrasound observations at PVC I on 28th February – 24th March 2021. Azimuth of
 495 signal arrival is shown; the colorbar refers to the signal trace velocity. Green background
 496 marks the streamer event, grey background marks the calm periods.

497

498 Changes of the trace velocity can indicate changes of the refraction altitude of the signal
 499 (Lonzaga, 2015). The exact limits of the trace velocity for the given atmospheric waveguide
 500 depend on the current state of the atmosphere. We use the thresholds determined for a
 501 model atmosphere in Lonzaga (2015) as helpful hints for our further consideration: Trace
 502 velocities below 0.340 km/s indicate signal refraction in the troposphere and lower
 503 stratosphere. Trace velocities between 0.340 and 0.380 km/s are typical for signals ducted
 504 in the waveguide between the ground and the upper stratosphere. Signals traveling in the
 505 thermospheric waveguide arrive with trace velocities larger than 0.380 km/s.

506 The high trace velocities recorded at PVC I disprove signal refraction in the lower
 507 stratosphere. Hence, it is unlikely that the signals arrive through a waveguide that can form
 508 at the tropopause – lower stratosphere by the effect of the streamer event.

509 Like in the November 2020 case, signal propagation above the eastern North Atlantic and
 510 Western and Central Europe is investigated using the InfraGA/GeoAc tools. Propagation of
 511 the 0.2 Hz signal is modelled ~~on~~for 10th March at 03 UTC, [in the middle of the streamer](#)

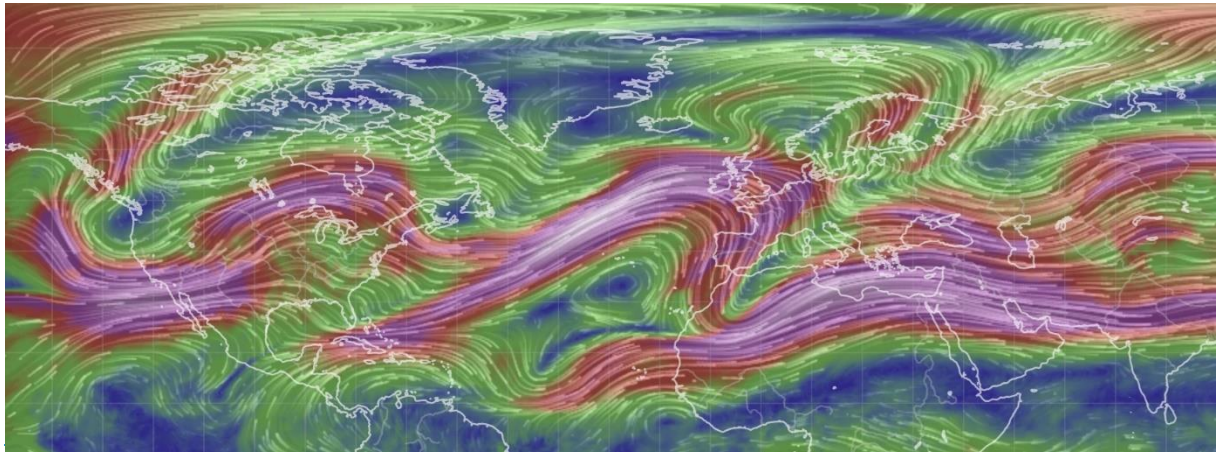
512 [event](#). A source is located at 55°N 15°W at a distance of ~2000 km from the stations. This
513 scenario represents signal propagation from the central North Atlantic. The other source is
514 located at 55°N 0°latitude representing propagation of microbaroms from the North Sea.
515 The distance from the stations is ~1000 km. [Both points are located under the jet-stream](#)
516 [disturbance related to a streamer event](#).

517 Eastward signal ducting is enabled in the stratospheric and thermospheric waveguides
518 from both sources to the stations. Strong signal absorption in the thermospheric waveguide
519 likely disables thermospheric arrivals to the PPCI and WBCI. We assume that signals
520 ducted in the upper stratosphere are detected. The other eastward waveguide occurs near
521 the tropopause, formed by the eastward to south-eastward jet-stream above the eastern
522 North Atlantic and Western Europe at latitudes 50 – 60°N (Figure 9-). Signals from the
523 source in the North Atlantic are predicted to travel in the tropopause waveguide to distances
524 of 1000-1100 km. The signal attenuation is low in the tropopause waveguide; the relatively
525 short distance under the waveguide influence is determined by the location and extent of
526 the jet-stream disturbance. The tropopause/lower stratosphere arrivals can be detected
527 mainly on the British Isles. The waveguide does not reach to PPCI and WBCI stations (see
528 supplementary materials).

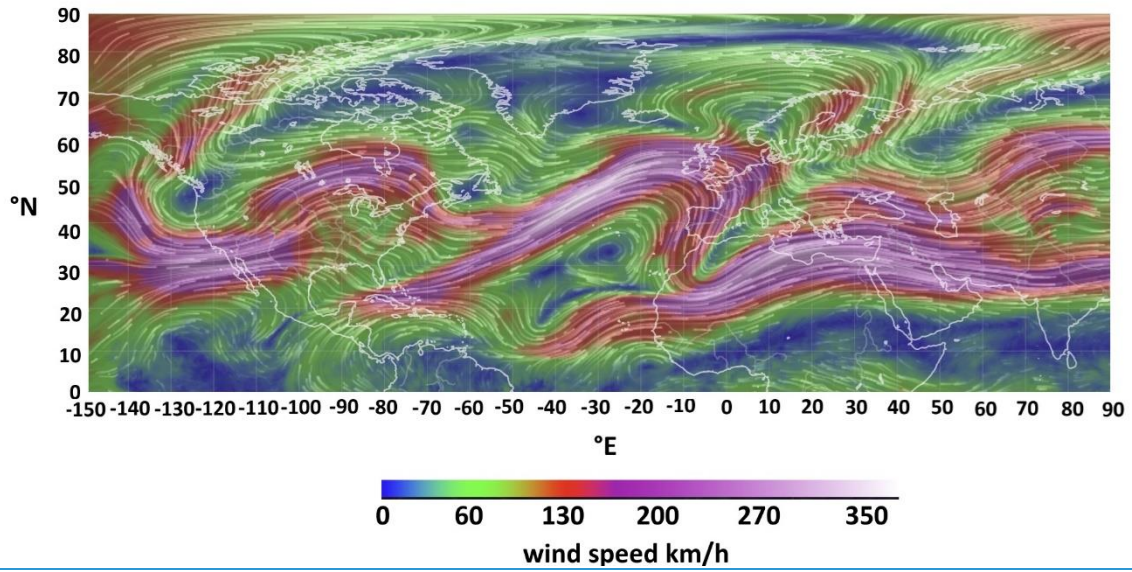
529 Signals emitted by a source in the North Sea can propagate through the tropopause
530 waveguide. The signals propagate to the south-east and are predicted to reach Central
531 Europe. The tropopause/lower stratosphere arrivals are represented by red dots in Figure
532 10. The influenced regions are to the south-west from PPCI and WBCI, several hundreds
533 of kilometres distant from the stations. The approximation of infrasound propagation
534 obtained from the raytracing is in accord with observations. The trace velocities at PPCI of
535 0.377 km/s indicate infrasound propagation in the waveguide formed between the ground
536 and the upper stratosphere rather than in the waveguide near the tropopause.

537 Like in the November 2020 case, infrasound arrivals from the North Atlantic to the
538 stations PPCI and WBCI in Central Europe are not influenced by the waveguide at the
539 tropopause – lower stratosphere. Observed trace velocities fluctuate within or close above
540 the limits that indicate infrasound propagation in the upper stratosphere during the streamer
541 event and both adjacent quiet periods.

542



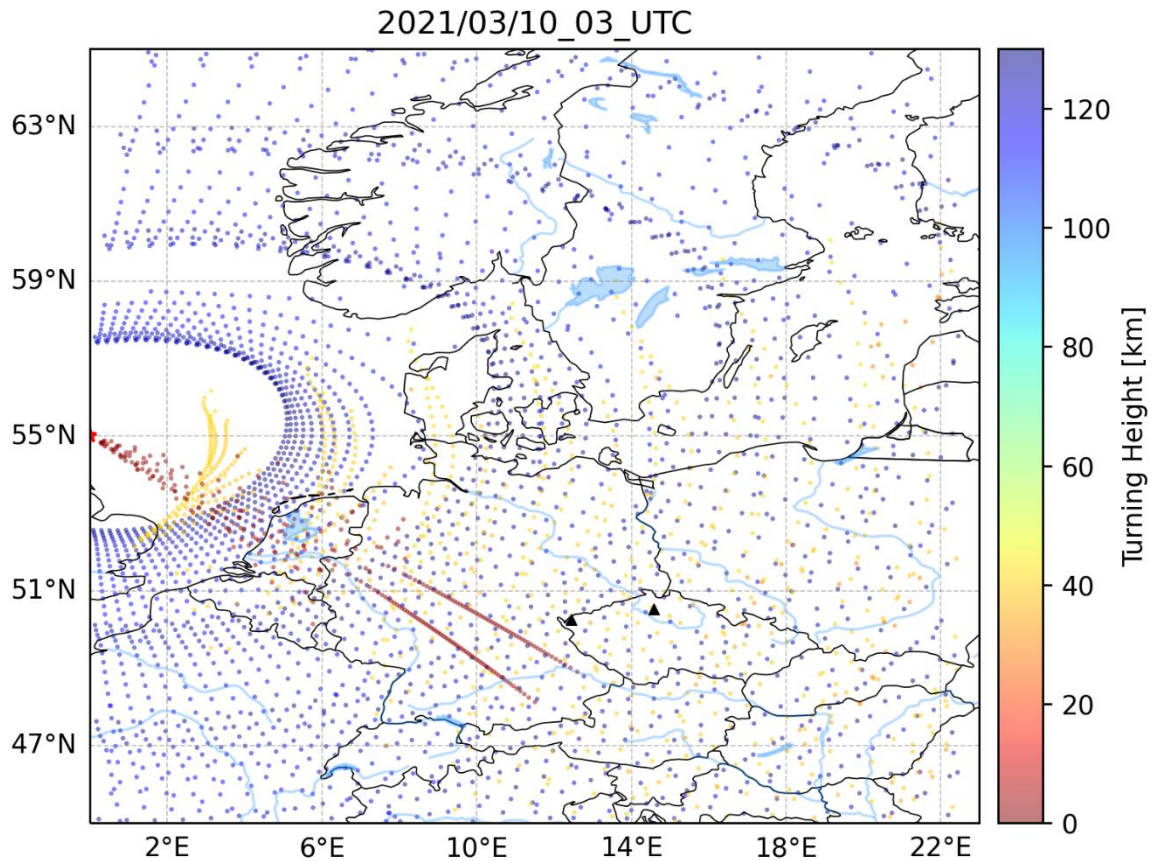
543



544

545 Fig.9. Wind field at the pressure level of 250 hPa on 10 March 2021 at 03 UTC. A
 546 disturbance of the jet-stream above the eastern North Atlantic and the British Isles is caused
 547 by the streamer event. [Figure taken from earth.nullschool.net](http://earth.nullschool.net)

548



549
 550 Fig.10 Modelled infrasound propagation from a point source located at 55°N and 0°longitude
 551 (red asterisk) on 10th March 2021 at 03 UTC. ~~Colorbar~~The colorbar refers to the turning height
 552 (maximum height) of the signal. Red color indicates signal propagation in the waveguide
 553 formed near the tropopause (altitudes around 10 km), arrivals through the stratospheric
 554 waveguide are shown in yellow (altitudes around 40-50 km) and arrivals through the
 555 thermospheric waveguide are shown in blue (altitudes above 100 km). Black triangles
 556 represent infrasound arrays WBCI (the left triangle) and PVICI (the right triangle).

557
 558

559 3.2 Results and discussion of gravity waves in the troposphere and ionosphere

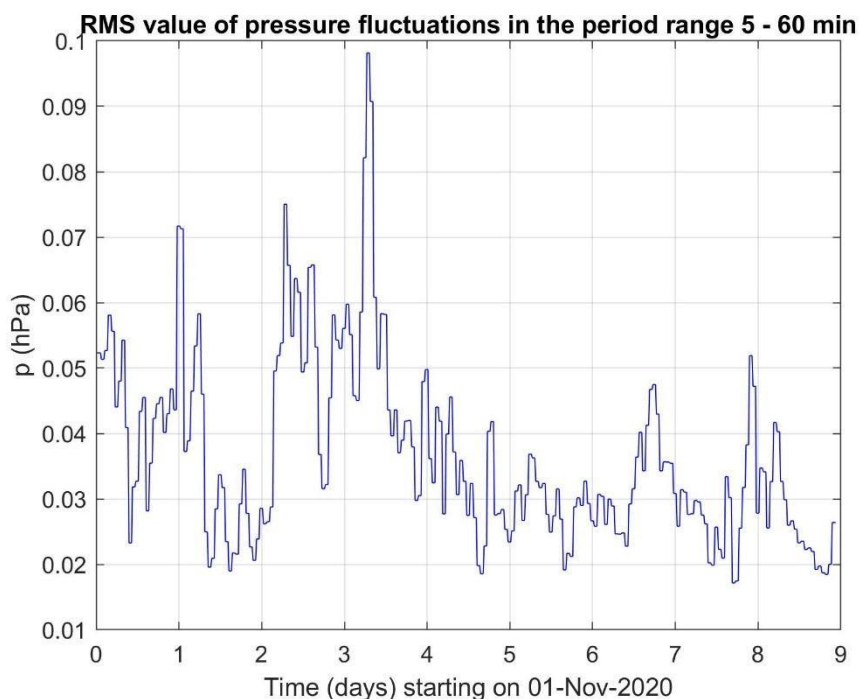
560

561 3.2.1 Investigation of GWs measured on the ground by WBCI array of micro- 562 barometers.

563 Figure 11 shows the RMS amplitudes of pressure fluctuations in the period range 5-60 min
 564 recorded from November 1 to November 9, 2020. This interval covers a distinct streamer
 565 event that occurred from November 3 to November 7. The results of propagation analysis are
 566 shown in Figure 12, which displays the phase velocities and azimuths of GWs. Only results

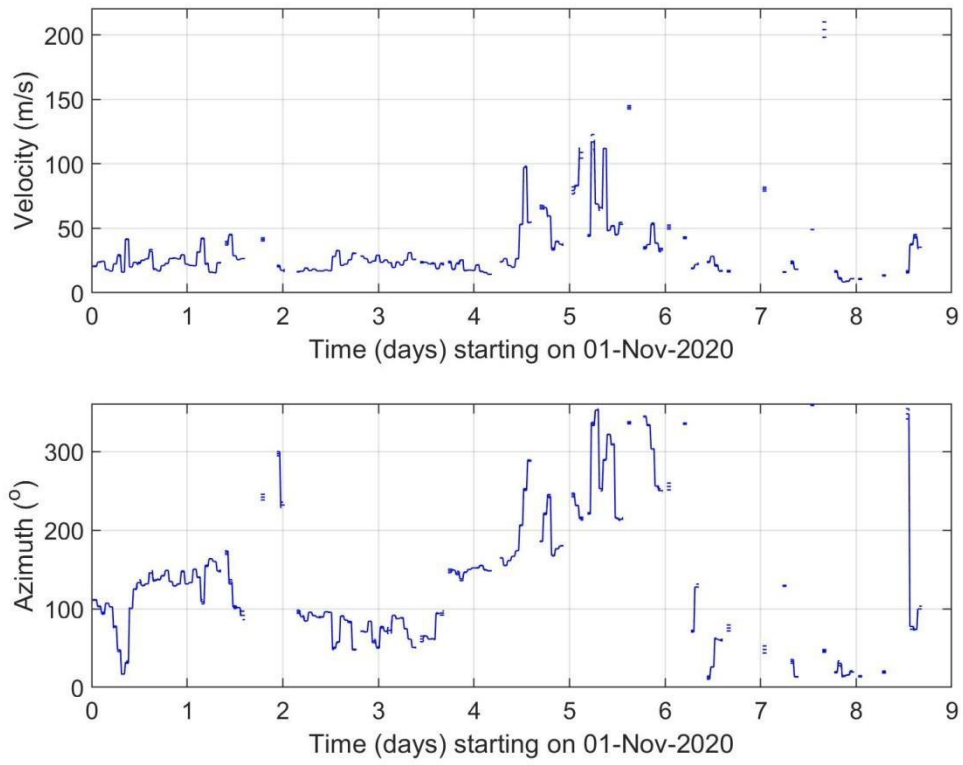
567 that satisfied the criterion ($dv/v < 0.5$) and ($dAZ < 10^\circ$) and ($p_{RMS} > 0.02$ Pa) are presented,
 568 where dv/v , dAZ , p_{RMS} are the relative uncertainty of GW phase velocity, uncertainty of
 569 azimuth and root mean square value of pressure fluctuations in the analysed time interval.
 570 Figure 12 demonstrates that there is a tendency for higher phase velocities and occurrence of
 571 different azimuths during the streamer event. Therefore, it is useful to compare the GW
 572 characteristics during streamer events and calm conditions.

573 Figure 13 shows histograms obtained by a statistical analysis. The RMS amplitudes of
 574 pressure fluctuations in the period range 5 – 60 min, phase velocities and azimuths were
 575 investigated separately for calm conditions (upper plots) and for streamer events listed in
 576 Table 1 (bottom plots) with a 1-hour time resolution. The solid vertical lines mark lower (Q1)
 577 and upper (Q3) quartiles. The dashed vertical lines depict boundaries for large ($Q3 + 1.5 \cdot (Q3 -$
 578 $Q1)$) and extreme ($Q3 + 3 \cdot (Q3 - Q1)$) values. A difference between histograms for RMS
 579 pressure fluctuations and azimuths obtained for calm and disturbed conditions is obvious.
 580 During the streamer events the azimuths are distributed more randomly and more extreme
 581 pressure amplitudes can be observed. A minor difference is also observed for phase
 582 velocities.



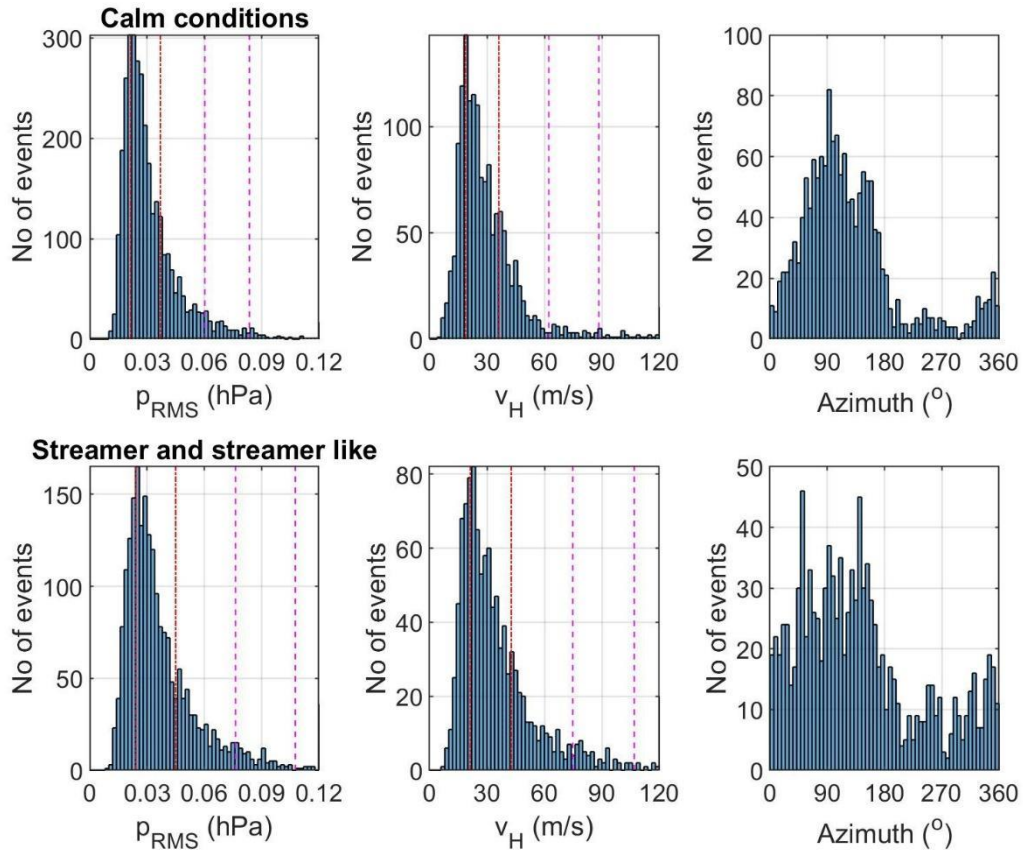
583

584 **Figure 11** Amplitude of GWs recorded by WBCI from 2020-11-01 to 2020-11-09



585

586 **Figure 12** Propagation velocity and azimuth of GWs recorded by WBCI from 2020-11-01 to
587 2020-11-09



588

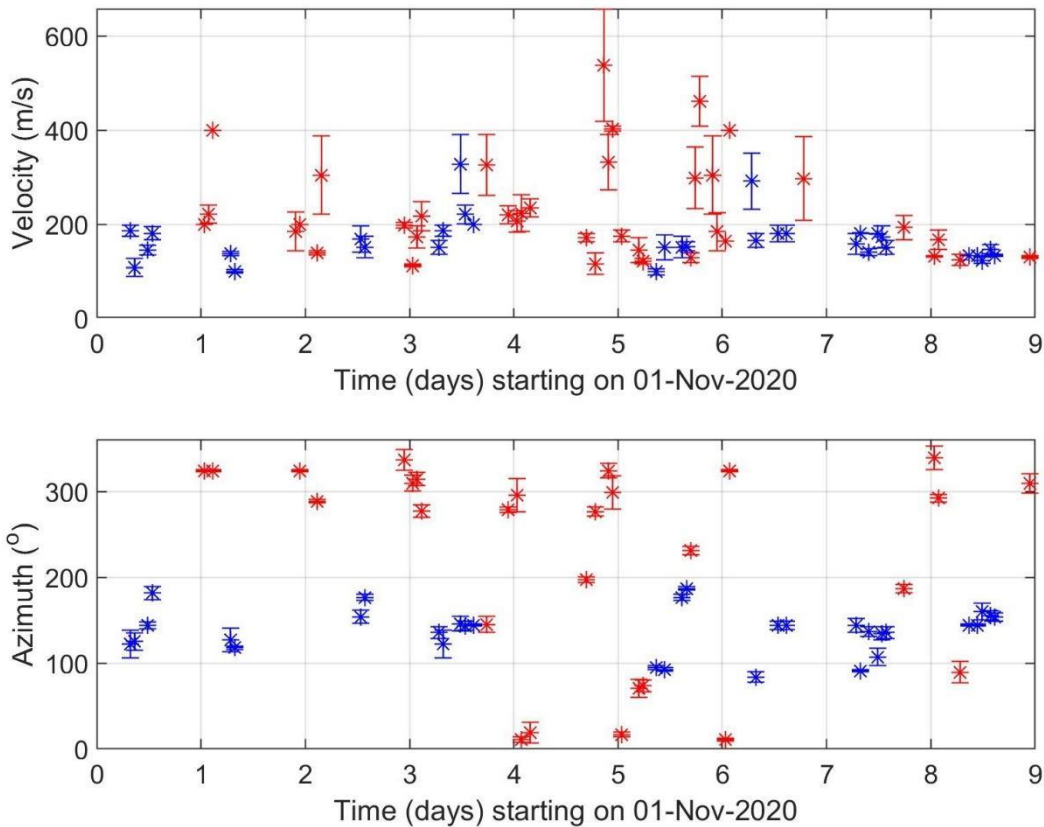
589 **Figure 13** GW characteristics (RMS of pressure fluctuations, phase velocity and azimuth)
 590 for calm periods (upper plots) and streamer and streamer like events (bottom plots) for 2020
 591 and winter 2021. The red vertical lines mark lower (Q1) and upper (Q3) quartiles. The dashed
 592 magenta vertical lines depict boundaries for large ($Q3 + 1.5 \cdot (Q3 - Q1)$) and extreme ($Q3 + 3 \cdot (Q3 -$
 593 $Q1)$) values.

594

595 3.2.2 Investigation of GWs measured in the ionosphere by continuous Doppler 596 sounding system (CDS)

597 The 2D propagation analysis of GWs was performed using the 2D versions of methods
 598 mentioned in Section 2 and in detail described by Chum and Podolská (2018). As discussed in
 599 Section 2 and by (Chum et al., 2021), the 2D propagation analysis makes it possible to
 600 analyze much larger number of time intervals than the 3D analysis. The propagation analysis
 601 obtained for the interval from 1st November to 9th November 2020, which covers the
 602 significant streamer event that occurred from 3rd November 2020 to 7th November 2020, is
 603 presented in Figure 14. Only results that satisfied the criteria ($dv/v < 0.2$) and ($dAZ < 20^\circ$) and

604 ($f_{\text{DRMS}} > 0.05$ Hz) and ($C_{\text{max}} < 0.5$) are presented, where dv/v is the relative uncertainty of GW
605 phase velocity, dAZ is the azimuth uncertainty, f_{DRMS} is the root mean square of the Doppler
606 shift in the analysed time interval and C_{max} is the maximum in the normalized energy map for
607 the best beam (slowness) search; C_{max} is 1 for identical signals (Chum and Podolská, 2018). It
608 is considered that signals are not sufficiently correlated (coherent) for reliable propagation
609 analysis if $C_{\text{max}} < 0.5$ (Chum et al., 2021). The velocities and azimuth obtained by observation
610 at 3.59 MHz are in red, whereas the values based on measurements at 4.65 MHz are in blue.
611 Obviously, the observations at 3.59 MHz mostly correspond to the nighttime, whereas
612 observations at 4.65 MHz were mostly made during the daytime. The 4.65 MHz signal did not
613 reflect from the ionosphere (escaped to the outer space) at night due to the low critical
614 frequency of the ionosphere. On the other hand, the 3.59 MHz signal mostly reflected during
615 the day from the ionospheric E layer and the Doppler shift was negligible, difficult to
616 analyse. The GWs usually propagated roughly poleward at night and roughly equatorward
617 during the daytime. This is fully consistent with the statistical investigation (Chum et al.,
618 2021) which showed that propagation directions of GWs in the ionosphere exhibit diurnal and
619 seasonal behaviour and are mainly controlled by the neutral winds in the thermosphere.



620

621 **Figure 14** Propagation velocity and azimuth of GWs in the ionosphere obtained using CDS
622 measurements from 2020-11-01 to 2020-11-09. The velocities and azimuth obtained by
623 observation at 3.59 MHz are by red, whereas the values based on measurements at 4.65 MHz
624 are by blue.

625 Based on the analysis of the GW observed in the ionosphere during the streamer event and
626 on the previous statistical analysis, we conclude that no obvious signature related to streamer
627 event was observed for the propagation of GW the ionosphere.

628 It should be also mentioned that the phase velocities of GW measured on the ground (Figure
629 8) and at heights around 200 km in the ionosphere differ. There are several reasons for that.
630 First, the observed horizontal phase velocities depend on the elevation angle of GW
631 propagation and on the ambient temperature as follows from the dispersion relation (the
632 temperature enters the dispersion relation via the buoyancy frequency and the scale height).
633 The temperature in the ionosphere/thermosphere is several times higher than in the
634 troposphere. The elevation angles might change during the upward propagation of GWs,
635 depending on the wind and temperature profile. Second, GWs propagate with a tilt, not
636 vertically upward. It is therefore highly probable that the sources of the GWs observed in the
637 troposphere and ionosphere are different. Moreover, GW can break during their propagation
638 upward and secondary gravity waves might be observed in the ionosphere.

639 **4) Conclusion and discussion**

640 The focus of this study was to test independent types of observations like Doppler sounding
641 and microbarograph measurements for an analysis of GW behavior during streamer events,
642 which are strongly connected with PW or GW and the large scale mass transport of ozone and
643 that is why it can be very interesting for studies of atmospheric dynamics.

644 We also ~~investigate effects of the streamer events on~~investigated infrasound propagation:
645 ~~Streamer events are significant disturbances to circulation in the tropopause/lower~~
646 ~~stratosphere region. Modifications~~ during streamer events, since modifications of infrasound
647 ducting in the atmosphere can ~~therefore~~ be expected. ~~Indeed, the~~ in these periods. We
648 ~~evaluated infrasound detections at two microbarograph arrays in Central Europe during~~
649 ~~streamer events and compared them with observation during adjacent quiet periods. To obtain~~
650 ~~an overview of infrasound propagation from the source region to the region of observations,~~
651 InfraGA/GeoAc raytracing tools ~~predict~~(Blom and Waxler, 2012; Blom, 2019) were
652 ~~employed. In general, geometric acoustic approximation (raytracing) and the full wave~~

653 [models are used for simulations of infrasound propagation through the atmosphere. The great](#)
654 [advantage of the full wave models is that they capture the leaking of energy between the](#)
655 [waveguides. Waxler and Assink \(2019\) emphasize particularly energy leaking between the](#)
656 [tropospheric and stratospheric waveguide. Geometrical acoustics approximation provides an](#)
657 [easy-to-interpret model of infrasound propagation in the atmosphere at lower computational](#)
658 [costs compared to the full wave models. Its disadvantage is that the geometrical acoustics](#)
659 [approximation assumes no energy propagation in the forbidden regions \(for details see e.g.](#)
660 [Waxler and Assink, 2019\) and thus provides a model of infrasound propagation in separated](#)
661 [waveguides. Available methods of infrasound propagation simulations are in detail discussed](#)
662 [by Waxler and Assink \(2019\). The approximation of atmospheric wave ducts provided by the](#)
663 [raytracing was sufficient for the purpose of our study; we aimed to obtain an elemental picture](#)
664 [of infrasound propagation during the periods of interest; it means to identify which wave](#)
665 [guides are formed, their directivity, and spatial extent.](#)

666 [The InfraGA/GeoAc predicts](#) that a waveguide develops at the tropopause during the
667 analyzed streamer events in November 2020 and in March 2021 the direction of which is
668 determined by the disturbed jet-stream ~~and varies from event to event~~. The tropopause
669 waveguide ducts infrasound up to distances of several hundreds to a thousand of km from the
670 source in a limited azimuth range. The azimuth sector of the extent of 50 – 60° is influenced
671 in the analysed cases.

672 In accord with the model predictions, [phenomena that can be unambiguously attributed to](#)
673 streamer event ~~related phenomena effects~~ were not found in infrasound ~~detection~~[detections](#) at
674 the infrasound stations PPCI and WBCI ~~in Central Europe~~ during the studied cases. ~~The~~[We](#)
675 [assume that the](#) observability of streamer event signatures in infrasound arrival parameters
676 ~~therefore strongly~~ depends on the mutual position of the source, the streamer event
677 disturbance of the tropopause jet-stream and the infrasound station. It can be recommended
678 for future studies to use a dense network of infrasound arrays that covers various directions
679 and distances from the streamer event. Due to the typical occurrence of the streamer events
680 over the North Atlantic, infrasound stations in Western Europe ~~can be~~[are](#) of particular interest.

681 Supplementary ground-based measurements of GW using the WBCI array in the troposphere
682 showed that GW propagation azimuths were more random during streamer and streamer-like
683 events compared to those observed during calm conditions as can be seen from the plots in
684 Figure 13. On the other hand, the GW propagation characteristics observed in the ionosphere

685 by CDS during streamer events did not differ from those expected for the given time period,
686 based on previous statistical studies (Chum et al., 2021).
687 The results therefore indicate that streamers in the stratosphere might lead to changes in wave
688 propagation in the troposphere. The impact on the ionosphere was not confirmed, but cannot
689 be excluded due to sparse and localized observations of GW activity. In general, to validate the
690 preliminary results obtained in this study, a denser measurement network and more streamer
691 events need to be analyzed.

692

693 **Data availability:**

694 ozone column measurements ([TO3TCO](https://atmos.eoc.dlr.de/)) which are available as a service by DLR at
695 <https://atmos.eoc.dlr.de/>

696 Ground to space model vertical atmospheric profiles were obtained at
697 <https://g2s.ncpa.olemiss.edu/>; accessed on 27 January – 4 February 2024

698

699 The WAVEWATCHIII[®] wave-action model data were accessed via ftp at
700 [polar.ncep.noaa.gov/waves/JCOMM/2020](ftp://polar.ncep.noaa.gov/waves/JCOMM/2020) on 13-14 March 2023.

701

702 The Deutscher Wetterdienst synoptic charts were accessed at
703 https://www2.wetter3.de/archiv_dwd_dt.html on 3 February 2024.

704

705 **Author contributions**

706 MK and LK create the idea of manuscript; JCh, MK, TS, LK, and KP suggest the datasets and
707 methods; TS, JCh, LK, KP and FT analyzed the data; MK wrote the manuscript draft; JCh,
708 TS, LK and KP reviewed and edited the manuscript.

709 **Competing interests**

710 The authors declare that they have no conflict of interest.

711

712 **Acknowledgement**

713 The DTK-GPMCC software was kindly provided by Commissariat à l'énergie atomique et
714 aux énergies alternatives, Centre DAM-Île-de-France, Département Analyse, Surveillance,
715 Environnement, Bruyères-le-Châtel, F91297 Arpajon, France.

716 The authors are grateful to Dr. Phil Blom and Los Alamos National Laboratory for opening
717 the InfraGA/GeoAc tools to the public.

718 [We also acknowledge earth.nullschool.net for providing the figures.](#)

719 **Financial support:** This study is supported by LISA project- Lidar measurements to
720 Identify Streamers and analyze Atmospheric waves, AEOLUS-INNOVATION, Contract No.
721 4000133567/20/I-BG

722

723 **References**

724 Assink, J.D., Waxler, R., Smets, P., Evers, L.G. (2014). Bidirectional infrasonic ducts
725 associated with sudden stratospheric warm-ing events. *J. Geophys. Res. Atmos.* 119,1140-
726 1153.

727 Bittner, M., Höppner, K., Pilger, C., Schmidt, C. (2010). Mesopause temperature
728 perturbations caused by infrasonic waves as a potential indicator for the detection of
729 tsunamis and other geo-hazards. *Nat. Hazards Earth Syst. Sci.*, 10, 1431-1442. [www.nat-](http://www.nat-hazards-earth-syst-sci.net/10/1431/2010/doi:10.5194/nhess-10-1431-2010)
730 [hazards-earth-syst-sci.net/10/1431/2010/doi:10.5194/nhess-10-1431-2010](http://www.nat-hazards-earth-syst-sci.net/10/1431/2010/doi:10.5194/nhess-10-1431-2010)

731 Blanc, E. (1985). Observations in the upper atmosphere of infrasonic waves from natural or
732 artificial sources: A summary. *Ann. Geophys.*, 3, 673-688.

733 Blixt, E.M., Nasholm, S.P., Gibbons, S.J., Evers, L.G., Charlton-Perez, A.J., Orsolini, Y.J.,
734 Kvaerna, T. (2019). Estimating tropo-spheric and stratospheric winds using infrasound from
735 explosions. *J. Acoust. Soc. Am.* 146:2.

736 Blom, P., Waxler, R. (2012). “Impulse propagation in the nocturnal boundary layer: Analysis
737 of the geometric component”. *J. Acoust. Soc. Am.*, **131**, 3680 – 3690. doi:

738 [10.1121/1.3699174](https://doi.org/10.1121/1.3699174).

739 Blom, P. (2019). “Modeling infrasonic propagation through a spherical atmospheric layer:
740 Analysis of the stratospheric pair.” *J. Acoust. Soc. Am.*, **145**, 2198–2208. doi:

741 [10.1121/1.5096855](https://doi.org/10.1121/1.5096855).

742 Bondár I., T. Šindelářová, D. Ghica, U. Mitterbauer, A.Liashchuk, J. Baše, J. Chum, C.
743 Czanik, C. Ionescu, C. Neagoe, M. Pásztor, A. Le Pichon (2022), Central and Eastern

744 European Infrasound Network: Contribution to Infrasound Monitoring, *Geophys. J. Int.*,
745 ggac066, <https://doi.org/10.1093/gji/ggac066>

746 Brachet, N., Brown, D., Le Bras R., Cansi, Y., Mialle, P., Coyne, J. (2010). Monitoring the
747 Earth's Atmosphere with the Global IMS Infrasound Network. In: Le Pichon, A., Blanc, E.,
748 Hauchecorne A. (Eds.), *Infrasound Monitoring for Atmospheric Studies*. Springer
749 Science+Business Media B.V., 77-118. Doi: 10.1007/978-1-4020-9508-5_3

750 Campus, P., Christie, D.R. (2010). Worldwide Observations of Infrasonic Waves. In: Le
751 Pichon, A., Blanc, E., Hauchecorne A. (Eds.), *Infrasound Monitoring for Atmospheric*
752 *Studies*. Springer Science+Business Media B.V., 185234-118. Doi: 10.1007/978-1-4020-
753 9508-5_6

754 Cansi, Y., 1995. An automatic seismic event processing for detection and location: The
755 P.M.C.C. method. *Geophys. Res. Lett.* 22, 1021-1024. doi: 10.1029/95GL00468

756 Ceranna, L., Matoza, R., Hupe, P., Le Pichon, A., Landès, M., (2019). Systematic Array
757 Processing of a Decade of Global IMS Infrasound Data. In: Le Pichon, A., Blanc, E.,
758 Hauchecorne, A. (eds) *Infrasound Monitoring for Atmospheric Studies*. Chal-lenges in
759 *Middle Atmospheric Dynamics and Societal Benefits*. Springer Nature Switzerland AG.

760 Chum J, Podolská K (2018) 3D analysis of GW propagation in the ionosphere. *Geophysical*
761 *Research Letters*, 45, 11,562–11,571, <https://doi.org/10.1029/2018GL07969>

762 Chum, J., Podolská, K., Rusz, J., Baše, J., Tedoradze, N. (2021), Statistical investigation of
763 gravity wave characteristics in the ionosphere. *Earth Planets Space* 73, 60,
764 <https://doi.org/10.1186/s40623-021-01379-3>

765 Czech microbarograph network, <https://doi.org/10.7914/SN/C9>

766 Drob, D. P., Picone, J. M., Garcés, M. (2003). Global morphology of infrasound propagation.
767 *J. Geophys. Res. Atmospheres*, **108** (D21). doi: [10.1029/2002JD003307](https://doi.org/10.1029/2002JD003307).

768 Evers, L. G., Siegmund, P. (2009). Infrasonic signature of the 2009 major sudden
769 stratosphericwarming, *Geophys. Res. Lett.*, 36, L23808, doi:10.1029/2009GL041323

770 Evers, L.G., Haak, H.W. (2010). The Characteristics of Infrasound, its Propagation and Some
771 Early History. In: Le Pichon, A., Blanc, E., Hauchecorne, A. (eds) *Infrasound Monitoring for*
772 *Atmospheric Studies*. Springer, Dordrecht.

773 Evers, L. G., van Geyt, A. R. J. , Smets, P., Fricke, J.T. (2012). Anomalous infrasound
774 propagation in a hot stratosphere and the existence of extremely small shadow zones, *J.*
775 *Geophys. Res.*, 117, D06120, doi:10.1029/2011JD017014.

776

777 Eyring, V., Dameris, M., Grewe, V., Langbein, I., & Kouker, W. (2002). Climatologies of
778 streamer events derived from a transport model and a coupled chemistry-climate model.

779 Fritts, D.C. & Alexander, M.J., (2003). Gravity wave dynamics and effects in the middle
780 atmosphere. *Rev. Geophys.*, 41 (1), 1003.

781 Garcès, M., Willis, M., Hetzer, C., Le Pichon , A., Drob, D., (2004). On using ocean swells
782 for continuous infrasonic measurements of winds and temperature in the lower, middle, and
783 upper atmosphere. *Geophys. Res. Lett.* 31, L19304. doi: 10.1029/2004GL020696

784 Garcès, M.A., (2013). On infrasound standards, part 1: Time, frequency, and energy scaling.
785 *InfraMatics* 2, 13-35. doi: 10.4236/inframatics.2013.22002

786 Georges, T.M. (1968). H. F. Doppler studies of travelling ionospheric disturbances. *J.*
787 *Atmos.Terr. Phys.*, 30, 735-746.

788 Gerlach, C., Földvary, L., Švehla, D., Gruber, T., Wermuth, M., Sneeuw, N., ... &
789 Steigenberger, P. (2003). A CHAMP-only gravity field model from kinematic orbits using the
790 energy integral. *Geophysical Research Letters*, 30(20).

791 Hersbach, H., Bell, B., Berrisford, P., Hirahara, S., Horányi, A., Muñoz-Sabater, J., ... &
792 Thépaut, J. N. (2020). The ERA5 global reanalysis. *Quarterly Journal of the Royal*
793 *Meteorological Society*, 146(730), 1999-2049.

794 Hupe, P., Ceranna, L., Pilger, C., de Carlo, M., Le Pichon, A., Kaifler, B., Rapp, M. (2019).
795 Assessing middle atmosphere weather models using infrasound detections from microbaroms.
796 *Geophys. J. Int.*, 216, 1761–1767 doi: 10.1093/gji/ggy520

797 James, P. M. (1998): A climatology of ozone mini-holes over the Northern Hemisphere.
798 International Journal of Climatology: A Journal of the Royal Meteorological Society, 18, 12:
799 12871303

800 Kramer, R., S. Wüst, and M. Bittner (2016). Investigation of gravity wave activity based on
801 operational radiosonde data from 13 years (1997-2009): Climatology and possible induced
802 variability, Journal of Atmospheric and Solar-Terrestrial Physics 140, 23–33;
803 <http://dx.doi.org/10.1016/j.jastp.2016.01.014>

804 Kramer, R., S. Wüst, C. Schmidt, and M. Bittner (2015). Gravity wave characteristics in the
805 middle atmosphere during the CESAR campaign at Palma de Mallorca in 2011/2012: Impact
806 of extratropical cyclones and cold fronts, Journal of Atmospheric and Solar-Terrestrial
807 Physics 128 (2015) 8–23, <http://dx.doi.org/10.1016/j.jastp.2015.03.001>

808 Kai Ming Huang, Shao Dong Zhang, Fan Yi, (2010). Reflection and transmission of
809 atmospheric gravity waves in a stably sheared horizontal wind field, Journal of Geophysical
810 Research: Atmospheres, 10.1029/2009JD012687, 115, D16,

811 Landès, M., Ceranna, L., Le Pichon, A., & Matoza, R. S. (2012). Localization of microbarom
812 sources using the IMS infrasound network. Journal of Geophysical Research:
813 Atmospheres, 117(D6).

814 Le Pichon, A., Cansi, Y. (2003). PMCC for infrasound data processing. InfraMatics 02, 1-9.

815 Le Pichon, A., Blanc, E., (2005). Probing high-altitude winds using infrasound. J. Geophys.
816 Res., 110, D20104. doi: 10.1029/2005JD006020

817 Le Pichon, A., Ceranna, L., Garcès, M., Drob, D., Millet, C., (2006). On using infrasound
818 from interacting ocean swells for global continuous measurements of winds and temperature
819 in the stratosphere. J. Geophys. Res., 111, D11106. doi: 10.1029/2005JD006690

820 Le Pichon, A., Vergoz, J., Blanc, E., Guilbert, J., Ceranna, L., Evers, L., Brachet, N., (2009).
821 Assessing the performance of the International Monitoring System's infrasound network:
822 Geographical coverage and temporal variabilities. J. Geophys. Res. 114, D08112. doi:
823 10.1029/2008JD010907

824 Leovy, C. B., Sun, C. R., Hitchman, M. H., Remsberg, E. E., Russell III, J. M., Gordley, L.
825 L., ... & Lyjak, L. V. (1985). Transport of ozone in the middle stratosphere: Evidence for
826 planetary wave breaking. *Journal of Atmospheric Sciences*, 42(3), 230-244.

827 Lonzaga, J.B., (2015). A theoretical relation between the celerity and trace velocity of
828 infrasonic phases, *J. Acoust. Soc. Am.*, 138, EL242-EL247.
829 <http://dx.doi.org/10.1121/1.4929628>

830 Loyola D.G., Koukouli M.E., Valks P., Balis D.S., Hao N., van Roozendaal M., Spurr R.J.D.,
831 Zimmer W., Kiemle S., Lerot C., Lambert J.-C. (2011) The GOME-2 total column ozone
832 product: Retrieval algorithm and ground-based validation, *Journal of Geophysical Research*,
833 vol. 116, D07302, Wiley-Blackwell

834 Marty, J., (2019). The IMS Infrasound Network: Current Status and Technological
835 Developments, in: Le Pichon, A., Blanc, E., Hauchecorn, A. (Eds.), *Infrasound Monitoring*
836 *for Atmospheric Studies. Challenges in Middle Atmosphere Dynamics and Societal Benefits.*
837 Springer Nature Switzerland AG, pp. 3–62. doi:10.1007/978-3-319-75140-5_1

838 McIntyre, M. E., & Palmer, T. N. (1983). Breaking planetary waves in the stratosphere.
839 *Nature*, 305(5935), 593-600.

840 Munro, R., Eisinger, M., Anderson, C., Callies, J., Corpaccioli, E., Lang, R., ... & Albinana,
841 A. P. (2006, June). GOME-2 on MetOp. In *Proc. of The 2006 EUMETSAT Meteorological*
842 *Satellite Conference, Helsinki, Finland (Vol. 1216, p. 48).*

843 Munro, R., et al. (2016): The GOME-2 instrument on the Metop series of satellites:
844 instrument design, calibration, and level 1 data processing – an overview, *Atmos. Meas.*
845 *Tech.*, 9, 1279–1301, <https://doi.org/10.5194/amt-9-1279-2016>.

846 Peters, D., Hoffmann, P., & Alpers, M. (2003). On the appearance of inertia-gravity waves on
847 the north-easterly side of an anticyclone. *Meteorologische Zeitschrift*, 12(1), 25-35

848 Polvani, L. M., & Plumb, R. A. (1992). Rossby wave breaking, microbreaking, filamentation,
849 and secondary vortex formation: The dynamics of a perturbed vortex. *Journal of Atmospheric*
850 *Sciences*, 49(6), 462-476.

851 Pramitha, M., Venkat Ratnam, M., Taori, A., Krishna Murthy, B. V., Pallamraju, D., and
852 Vijaya Bhaskar Rao, S. (2015). Evidence for tropospheric wind shear excitation of high-

853 phase-speed gravity waves reaching the mesosphere using the ray-tracing technique, *Atmos.*
854 *Chem. Phys.*, 15, 2709–2721, <https://doi.org/10.5194/acp-15-2709-2015>.

855 Rauthe, M., Gerding, M., Höffner, J., & Lübken, F. J. (2006). Lidar temperature
856 measurements of gravity waves over Kühlungsborn (54° N) from 1 to 105 km: A winter-
857 summer comparison. *Journal of Geophysical Research: Atmospheres*, 111(D24).

858

859 Wüst, S., & Bittner, M. (2006). Non-linear resonant wave–wave interaction (triad): Case
860 studies based on rocket data and first application to satellite data. *Journal of atmospheric and*
861 *solar-terrestrial physics*, 68(9), 959-976.

862

863 Wüst, S., Offenwanger, T., Schmidt, C., Bittner, M., Jacobi, C., Stober, G., Yee, J.H.,
864 Mlynczak, M. G. & Russell III, J. M. (2018). Derivation of gravity wave intrinsic parameters
865 and vertical wavelength using a single scanning OH (3-1) airglow spectrometer. *Atmospheric*
866 *Measurement Techniques*, 11(5), 2937-2947.

867

868 Smets, P.S.M., Evers, L.G. (2014). The life cycle of a sudden stratospheric warming from
869 infrasonic ambient noise observations, *J. Geophys. Res. Atmos.*, 119, 12,084-12,099

870 Spurr, R., Loyola, D., Heue, K. P., Van Roozendael, M., & Lerot, C. (2022). S5P/TROPOMI
871 Total Ozone ATBD. Deutsches Zentrum für Luft- und Raumfahrt (German Aerospace
872 Center), Weßling, Germany, Tech. Rep. S5P-L2-DLR-ATBD-400A.

873 Sutherland, L.C., Bass, H.E., (2004). Atmospheric absorption in the atmosphere up to 160
874 km. *J. Acoust. Soc. Am.*, 115, 1012–1032. <https://doi.org/10.1121/1.1631937>

875 Szuberla, C.A.L., Olson, J.V., (2004). Uncertainties associated with parameter estimation in
876 atmospheric infrasound rays. *J. Acoust. Soc. Am.* 115, 253-258. doi: 10.1121/1.1635407

877 Veefkind, J. P., Aben, I., McMullan, K., Förster, H., De Vries, J., Otter, G., ... & Levelt, P. F.
878 (2012). TROPOMI on the ESA Sentinel-5 Precursor: A GMES mission for global
879 observations of the atmospheric composition for climate, air quality and ozone layer
880 applications. *Remote sensing of environment*, 120, 70-83.

881 [Waxler, R., Assink, J., 2019. Propagation Modeling Through Realistic Atmosphere and](#)
882 [Benchmarking, in: Le Pichon, A., Blanc, E., Hauchecorn, A. \(Eds.\), *Infrasound Monitoring*](#)

883 [for Atmospheric Studies. Challenges in Middle Atmosphere Dynamics and Societal Benefits.](#)

884 [Springer Nature Switzerland AG, pp. 3–62. doi:10.1007/978-3-319-75140-5_15](#)

885

886